



Spatio-temporal surface temperature variations detected by satellite thermal infrared images at Merapi volcano, Indonesia

Hai-Po Chan ^{a,*}, Kostas I. Konstantinou ^a, Matthew Blackett ^b

^a Department of Earth Sciences and Graduate Institute of Geophysics, National Central University, Taoyuan City, Taiwan

^b School of Energy, Construction & Environment, Coventry University, Coventry, UK



ARTICLE INFO

Article history:

Received 18 May 2021

Received in revised form 10 September 2021

Accepted 19 September 2021

Available online 25 September 2021

Keywords:

Merapi volcano

Land surface temperature (LST)

Seasonal and Trend decomposition using LOESS (STL)

Landsat

MODIS

ASTER

ABSTRACT

Merapi volcano is located in central Java and is the most active volcano in Indonesia. Many thousands live on the volcano's flanks which itself is 28 km (17 mi) north of Yogyakarta and its 2.4 million inhabitants. Given this population at risk, and a history of 73 recorded eruptions in the past 500 years, the hazards posed by Merapi are worthy of study. Merapi is monitored by networks of on-site seismology, deformation, and gas emission instruments and, like all volcanoes globally, is also routinely observed by satellite remote sensors. Here, we conduct a temporal and spatial time series analysis of land surface temperature (LST) observations of Merapi, as derived from MODIS (1 km spatial resolution), ASTER (90 m) and Landsat (30 m) thermal infrared imagery. The time series derived from MODIS is decomposed with the Seasonal Trend Decomposition using a Loess (STL) technique and this reveals thermal anomaly peaks caused by the eruptions and a subtle rising tendency in LST since the launch of MODIS in 2000. ASTER surface temperature time series is used for the cross validation of the MODIS LST time series and again, demonstrates thermal anomaly peaks and a longer term upward trend. For a detailed delineation of thermal features at Merapi, the 30 m pixel Landsat thermal imagery derived brightness temperature (BT) distribution during the period from 1988 to 2019 is presented. Finally, change detections (i.e., pixel-by-pixel comparison) of BT distribution from 1988 to 2019 are performed to inspect the spatial temperature variations of Merapi volcano. Positive thermal anomaly areas are identified and these correspond to local heat sources revealed by seismic imaging and resistivity tomography. In summary, the satellite remote sensing approach provides insights into thermal features at a higher spatial and temporal scale than has been conducted in the past and these observations complement ongoing ground-based measurements. The results of this study will feed into both an enhanced understanding of Merapi's thermally anomalous subsurface structures and facilitation of volcano monitoring and hazard assessment.

© 2021 Elsevier B.V. All rights reserved.

1. Introduction

Mount Merapi is a stratovolcano rising to 2968 m on Central Java (Fig. 1). Among the 129 active volcanoes documented by the Center for Volcanology and Geological Hazard Mitigation (CVGHM) in Indonesia, Merapi is the most active with 73 historically observed eruptions since 1548 (CVGHM, 2019; GVP, 2013; Voight and Davis, 2000). It is also one of the Decade volcanoes listed by the International Association of Volcanology and Chemistry of the Earth's Interior (IAVCEI) in the 1990s, suggesting that its further study is important considering scales of historical eruptions and threats to inhabitants. Numerous research endeavors have been undertaken in this volcano. For instance, the previous research efforts have been collected in a landmark special

issue "Merapi volcano" in the Journal of Volcanology and Geothermal Research (vol. 100; 2000) (Gertisser et al., 2012).

Merapi is the youngest volcano of the volcanic group in southern Java, which has been formed due to the subduction of the Indo-Australian plate (underplate) and Sunda plate (upperplate) (Chadwick et al., 2007; Hamilton, 1979). Stratigraphic radiocarbon dating reveals that eruptions at Merapi from 400,000–10,000 years ago were mainly effusive and basaltic. However, since around 10,000 years ago, explosive eruptions have become dominant and viscous andesitic lavas regularly form lava domes. Merapi's eruptive history shows that lava-dome extrusion, dome-collapse, and column-collapse pyroclastic flows were the major activities in the 19th and 20th centuries (Camus et al., 2000; Darmawan et al., 2018; Gertisser et al., 2012; Newhall et al., 2000). In the 1800s, explosive eruptions of up to a VEI (in full) 4 were prevalent while into the 1900s, the effusive growth of viscous lava domes and lava flows became more common (Voight and Davis, 2000). The most destructive eruption in living memory occurred in

* Corresponding author.

E-mail addresses: haipochan@ncu.edu.tw (H.-P. Chan), kkonst@cc.ncu.edu.tw (K.I. Konstantinou), m.blackett@coventry.ac.uk (M. Blackett).

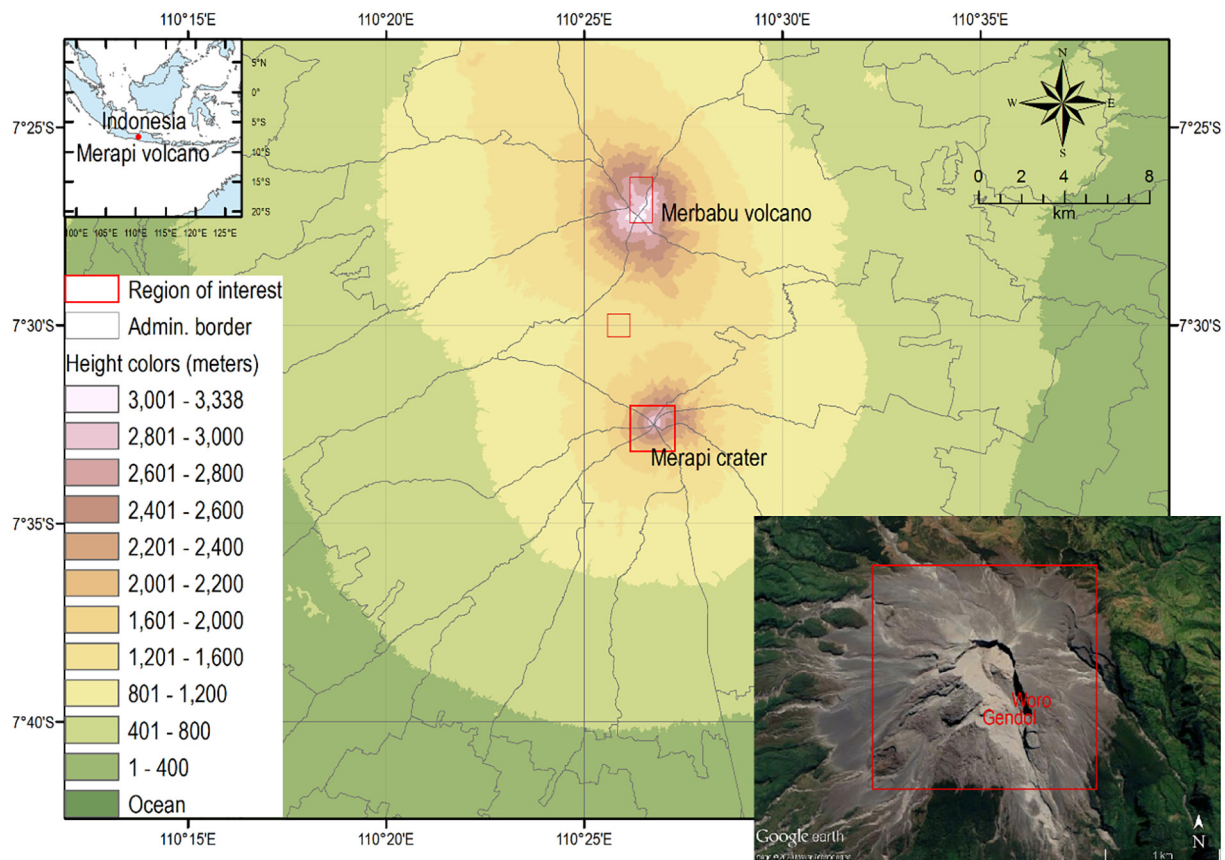


Fig. 1. Geography and DEM map of Merapi volcano, Indonesia. Volcano crater region of interest (ROI) and administrative boundaries are indicated. ROIs of the Merbabu crater and the saddle area in between the Merapi and Merbabu indicate the location of background temperature time series. The bottom right inset shows the Merapi crater zooming image from the Google Earth and the red text indicates the proximate location of Woro and Gendol fumarolic fields. (For interpretation of the references to colour in this figure legend, the reader is referred to the web version of this article.)

1930 with pyroclastic flows destroying thirteen villages and killing 1400 people. Into the twenty-first century, Merapi's behavior changed again, with 2010 witnessing a '100-year' event that constituted its largest and most explosive eruption series in more than a century. This eruption displaced at least a third of a million inhabitants and claimed nearly 400 lives (Jousset et al., 2012). The latest eruption occurred in the morning of May 11, 2018 (Volcanic Explosivity Index; VEI = 3), in which phreatic activity prompted a 5-km radius evacuation area around the volcano and forced the temporary shutdown of Yogyakarta's international airport (CVGHM, 2019).

Based on the listed eruption records at Merapi from the dataset on the Global Volcanism Program of the Smithsonian Institution, low-level activity (i.e., small eruptions; VEI = 1 or 2) regularly occurs every three to four years. However, the frequency of larger eruptions (VEI = 3 or 4) has increased in recent decades, with 3 eruptions of VEI > 3 since 2010. The higher frequency of larger intensity eruptions has seemingly generated more public-awareness at this active volcano based on the eruption records. In this context, this study aims to present longer-term monitoring of Merapi by using the three-decades (i.e., 1988–2020) of satellite remote sensing observation dataset.

Monitoring and assessing volcanic activity at Merapi is crucial for its hazard mitigation. The regular on-site seismic, gas emission, and deformation measurements, satellite-based remote sensing has been used for the study of Merapi. However, most remote sensing applications have focused on the individual eruptive events of 2006, 2010 and 2013, for instance and the surface temperature detection of the multiple phases of the 2006 Merapi eruption were studied using MODerate-resolution Imaging Spectroradiometer (MODIS) thermal infrared (TIR) imagery (Carr et al., 2016). Studies of regional earthquakes as triggers for

enhanced volcanic activity at Merapi, again based on evidence from MODIS thermal radiance data, were also studied (Harris and Ripepe, 2007). Assessment of volumetric change associated with the 2010 Merapi eruption was studied using satellite-based Interferometric Synthetic Aperture Radar (InSAR) data to generate DEMs of Merapi and to assess topographic changes caused by lava dome activities (Kubanek et al., 2015; Saepuloh et al., 2013; Walter et al., 2015). The volume estimation of the pyroclastic density current after the 2010 Merapi eruption was conducted using COSMO-SkyMed satellite X-band SAR data (Bignami et al., 2013) and satellite-derived InSAR observations were even used to understand precursory signals of the 2010 large eruption and to forecast eruptions hazards, and mitigate risks, at Merapi volcano (Saepuloh et al., 2013).

Given the myriad ways of monitoring and assessing volcanic activity, a holistic approach is required if we are to understand past and future behavior of active volcanoes. However, quantitative analysis on long-term eruptive behavior is often limited as such studies require long-term volcanic monitoring. Fortunately, remote sensing provides valuable information for decrypting the long-term volcanic mechanisms that may be hidden over short timescales. Here we use the global dataset archive of satellite imagery of Merapi from the Landsat and Terra/Aqua satellites operated by the National Aeronautics and Space Administration (NASA) and United States Geological Survey (USGS). We perform temporal and spatial monitoring analysis from the three-decade surface temperature time series retrieved from Terra/MODIS, Aqua/MODIS, Terra/ASTER and Landsat Thermal Infrared (TIR) images, with the aim of obtaining a deeper understanding of this volcano's past behavior and its future eruption trend, and thus being able to facilitate the effective mitigation on the possible subsequent hazards caused.

2. Materials and methods

In this study, 27 GB of imagery data from the NASA image archive has been processed. Satellite TIR images at Merapi volcano for the period 1988–2020 were selected based on the level of the image quality. More specifically, Landsat imagery products (originally 60 m spatial resolution, resampled to 30 m pixel size by default) and MODIS temperature products (1 km spatial resolution) were used for Merapi volcano monitoring. Landsat images are complementary—Landsat possesses a high spatial resolution but low temporal resolution in contrast to the high temporal resolution but low spatial resolution MODIS imagery. MODIS LST products are ready for use once downloaded while Landsat images require further post-processing. ASTER (The Advanced Spaceborne Thermal Emission and Reflection Radiometer) LST images with 90 m spatial resolution are also used for the validation of MODIS LST.

2.1. Landsat imagery derived brightness temperature

Images acquired from Landsat satellites and sensors (i.e., Landsat 5 TM and Landsat 7 ETM+) are used in this study. Landsat's multispectral sensors include TIR bands in the range: 10.40–12.50 μm . These wavelengths are specifically used to detect outgoing long-wavelength radiation from the Earth, the intensity of which largely depends on emitting surface temperature (Ahmad et al., 2002; Gupta, 2017). The sensors' design and operation are based on the principles of quantum mechanics that is applied by NASA. The overpass time for Landsat satellites is local time 10 to 10.30 am. The spatial and temporal resolutions are 30 m and 16 days, respectively (NASA, 2019).

We selected images of Merapi from different years and seasons based on Landsat Collection 1 LandsatLook Images of the USGS Global Visualization Viewer (GloVis) (USGS, 2021) (the criteria to select images is mainly based on the cloud cover) from the Landsat archives and from these retrieved the brightness temperature (BT) of the surface at Merapi. The BT is a measurement of the radiance of the electromagnetic radiation traveling from the Earth's surface to the satellite sensor at the top of the atmosphere (TOA), in temperature units of an equivalent black body. The BT is calculated by the inversion of the Planck function to the radiation measured. The BT and LST relate via the surface emissivity and atmospheric transmissivity, dictating that BT is always smaller than LST since surface emissivity in nature is less than one (Harris, 2013; Tang and Li, 2013). BT retrievals are much more effective than LST from the perspective of data processing because they omit complicated scene-specific atmospheric parameters and emissivity calculations (i.e., atmospheric correction). However, if the atmospheric correction is accounted for, the RMS error on corrected temperatures is around 2 °C (Barsi et al., 2003; Vidal et al., 1997).

Theoretically, the contribution of solar radiation at the TOA infrared radiation is negligible in the 8–14 μm wavelength both day and night, so the solar-related items, i.e., atmospheric scattering term (solar diffusion radiance), surface reflected downwelling atmospheric scattering term, and surface reflected downwelling solar beam term, in the thermal infrared radiative transfer equation (RTE) can be discarded without accuracy loss (Li et al., 2013). However, the solar radiation transmitted from the Sun to Earth is absorbed by the Earth's surface. It is then converted to heat and reemitted in the form of infrared to space (i.e., terrestrial radiation). The empirical study shows a linear relationship between the values of the shaded relief and LST, basically, the more shadows in a surface area the lower the LST values (Peng et al., 2020). An analysis study on factors affecting mountainous LST in the summer shows that land surface moisture characteristic is the main factor influencing the LST (Sun et al., 2014). Also, the angle of incoming solar radiation affects temperatures of locations at different latitudes. The solar radiation is more intense per unit of area when the sun's rays arrive Earth's surface near the equator, causing warmer temperatures. Thus consider the low latitude of the Merapi volcano (-7.5°) and the surface homogeneity in crater ROI area. The solar radiation effect on land surface can be averaged out while deriving the trend of BT temperature time series.

The Landsat data processing steps, including radiometric calibration, thermal band selection, and image classification, are summarised in Fig. 2 and more detailed procedures and result validation regarding the data processing are explained in the previous studies (Artis and Carnahan, 1982; Chan and Chang, 2018; Chan et al., 2017; Harris, 2013). BT is computed from a single channel algorithm based on the Planck radiation equation, which relates the rate at which a surface radiates energy to a function of kinetic temperature. However, BT is usually used in thermography because there is a certain relationship between brightness and kinetic temperatures (Artis and Carnahan, 1982). The accuracy of the BT retrieval is generally better than 2 K based on the experiment of ground-truth validation with meteorological temperature data from Central Weather Bureau (CWB) of Taiwan (Chan et al., 2017).

2.2. MODIS 8-day temperature products

In contrast to Landsat imagery, MODIS provides shorter revisit period (sub-daily) but at a rather coarse (1 km) spatial resolution. Here, data from the MODIS 8-day nighttime temperature data (Product ID: MOD11A2, MYD11A2) for 2000–2020 was used for time series analysis. The MOD11A2 (from Terra/MODIS) and MYD11A2 (from Aqua/MODIS) products are the 8-day average LST of the corresponding daily LST pixels, which is calculated from the nighttime observations and algorithms based on MODIS TIR bands (wavelength: 3.6–12.3 μm) (Wan, 2014; Wan and Li, 1997). The accuracy of the LST product is generally better than 1 K (0.5 K in most cases) based on the statement of the MODIS land team of NASA (NASA, 2018). To assess the quality of a 1 km by 1 km pixel resolution, an exemplary MODIS LST imagery in Merapi crater is shown in Fig. 3. The mean temperature difference is generally less than 1 K based on the previous comparison on the statistics of retrieved Landsat LST and MODIS LST product (Chan et al., 2017).

2.3. ASTER surface temperatures

ASTER is one of five imaging sensors onboard the Terra satellite launched in 1999 as a portion of NASA's Earth Observing System (NASA, 2020). ASTER is the only high spatial resolution sensor on the Terra satellite and, in effect, serves as a 'zoom' lens for the other sensors and as such, is particularly helpful for studies and applications on the land surface, change detection, and calibration or validation. Generally, the other sensors aboard Terra collect data daily. However, ASTER has a revisit time of 16 days, in stark contrast to sub-daily MODIS observations. ASTER acquires data in 14 spectral bands of the electromagnetic spectrum ranging from visible to TIR wavelength, namely, the visible and near infrared subsystem, the short wave infrared subsystem, and the TIR subsystem. Here, ASTER 90 m resolution surface temperatures at Merapi crater are derived from TIR images and used for the cross-validation of the MODIS LST.

2.4. STL decomposition

The task of deconstructing a time series into several components is termed decomposition, with each resulting component representing different data categories. Here, we utilize the "Seasonal and Trend decomposition using Loess (STL)" technique for decomposing the MODIS LST time series, while Loess is the method to estimate nonlinear relationships in the time series (Cleveland et al., 1990; Hafen, 2010). These techniques are capable of estimating nonlinear relationships within a dataset and have the advantage of handling seasonality and of being robust to outliers. STL divides up the time series into three parts: the trend, the seasonality, and the remainder. The occasional unusual observation generally does not affect the estimates trend and seasonal components, however, outliers do have an effect on the remainder component.

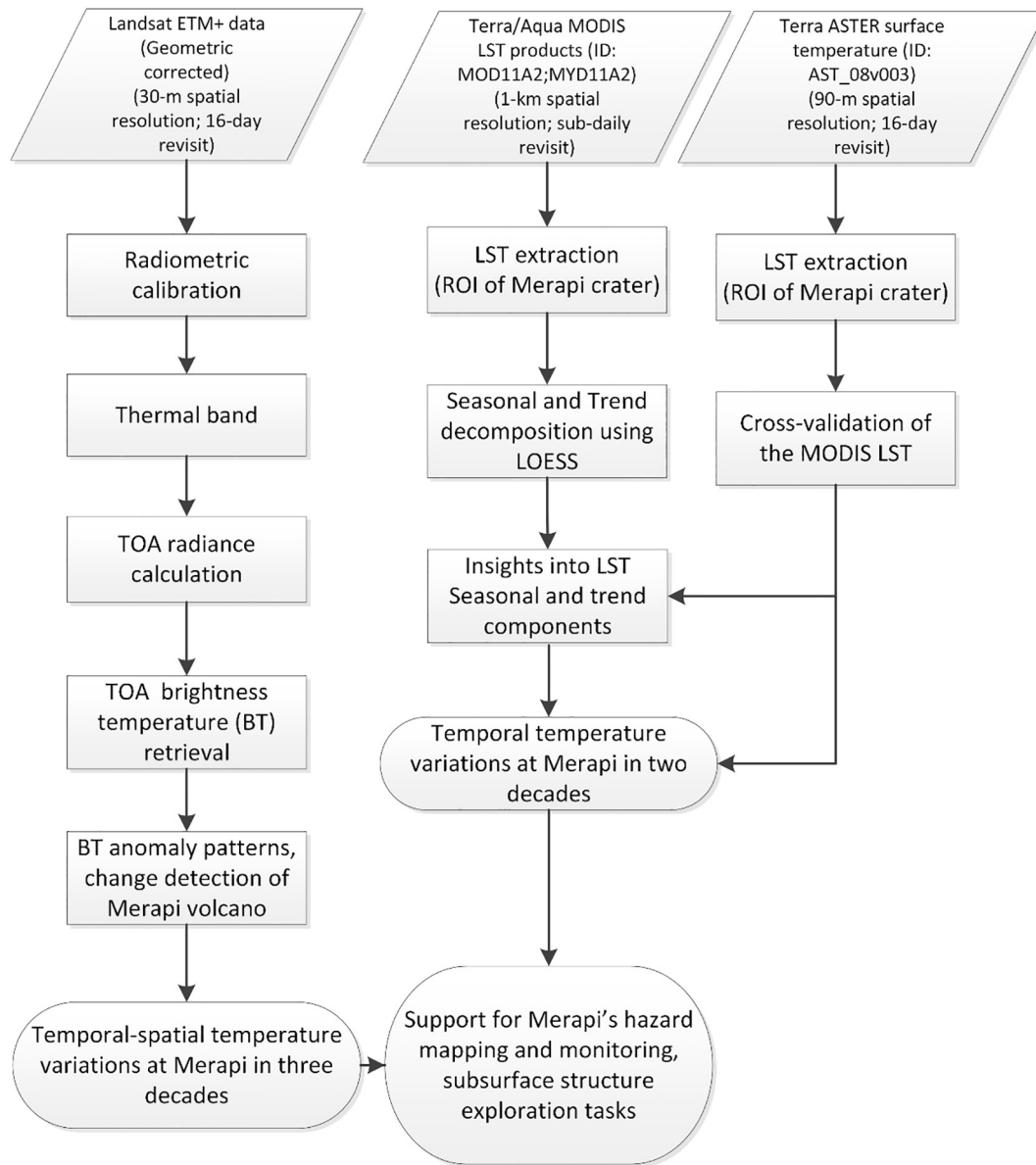


Fig. 2. Flow chart of Landsat, MODIS, and ASTER data processing and procedures conducted in this study. Three satellite TIR imagery datasets, namely, Landsat (Chan et al., 2017; Sobrino et al., 2008), MODIS and ASTER, are used.

3. Results

3.1. Monitoring Merapi crater with 8-day average MODIS LST products (2000 to 2020)

The MODIS 8-day average nighttime LST time series for Merapi crater (the region outlined in Fig. 3), March 2000–June 2020 is displayed in Fig. 4. It will be noted that there are numerous missing values and these relate to cloud and/or volcanic eruption plumes obscuring the surface from view. Indeed, there is a seasonal pattern which relates to the region's rainy season and there are data gaps during eruption events. Fig. 5 illustrates the background temperature time series of adjacent areas nearby to the Merapi crater (in Fig. 1) to show the differences of these MODIS LST time series compared with Merapi. In both regions there is an upward trend. However, the Merapi LST time series displays multiple thermal peaks caused by the eruption events, demonstrating that the Merapi crater LST is contributed to by volcanic origins as well as just the background characteristics. An independent *t*-test with a 5% significance level, confirms that the means of both sets of LST time series are significantly

different from each other. The null hypothesis is that the two sets of LST time series are from populations with equal means. Hypothesis test results (very small values of *p*) from both sets indicate the rejection of the null hypothesis at the Alpha (5%) significance level (see Table 1).

One significant advantage of STL decomposition is that it can handle missing data values in a time series and as such, it was applied to this MODIS LST time series (Fig. 6). The seasonality, trend and remainder components of the MODIS LST time series that resulted from the STL decomposition are evident. The Fourier transform has been applied to derive the dominant period for seasonality, and trend component. The dominant periods for seasonal and trend are 1.02 years and 10.2 years, respectively. The remainder component is what is left over when the seasonal and trend-cycle components are subtracted from the data and represents observable estimates of other information such as atmospheric circulation, El Niño phenomenon, meteoric cycle and others (Huang and Wu, 2008). The magnitude of seasonal and trend components is rather small compared to that of the remainder component. However, the retrieved seasonal period (i.e., 1.02 years) is close to the surface temperature annual cycle, indicating that STL works well in this instance.

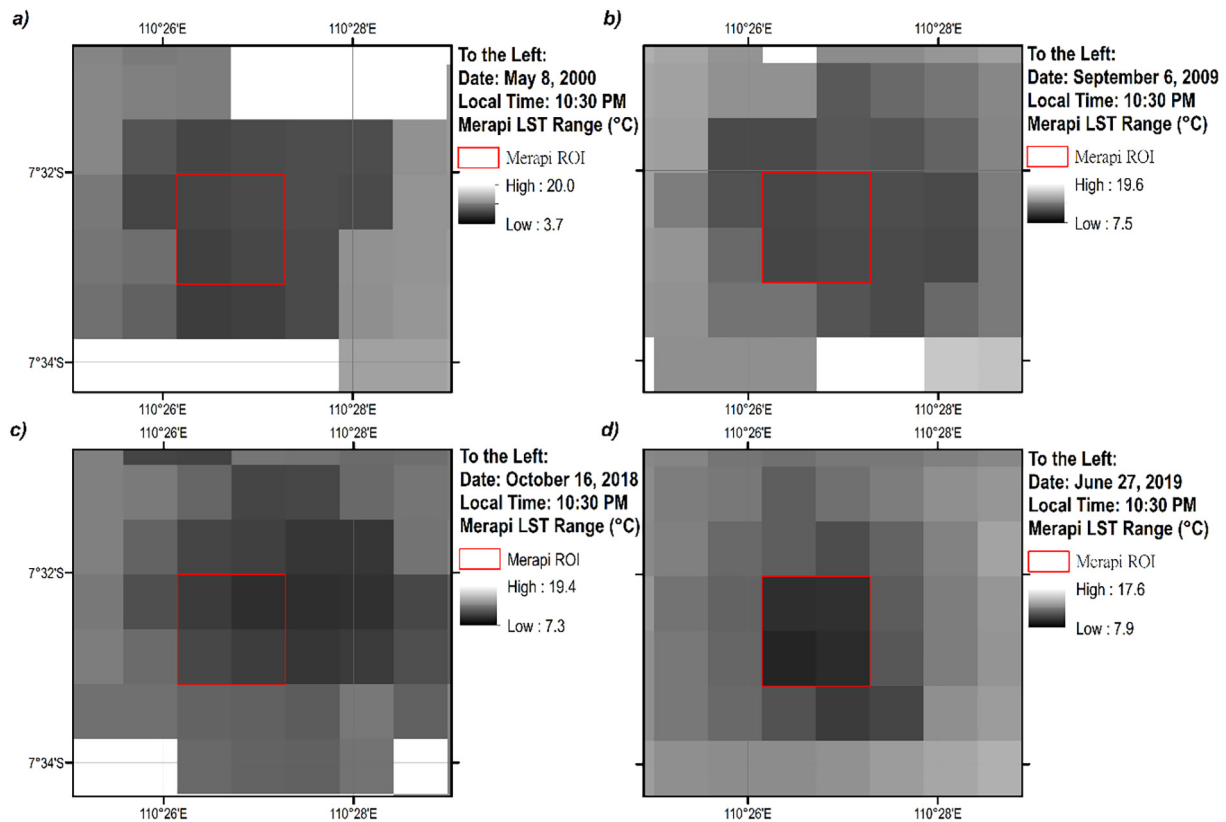


Fig. 3. The MODIS LST images (Product ID: MOD11A2) of 1 km by 1 km pixel size in the Merapi crater. The areas of Merapi crater (four pixels in the crater zone) are illustrated by the red colour box region in each image. The maximum temperature value among the four pixels are extracted as the crater LST. (For interpretation of the references to colour in this figure legend, the reader is referred to the web version of this article.)

3.2. Cross validation: Surface temperature time series at Merapi crater obtained from ASTER imagery

Fig. 7 shows the 90 m spatial resolution ASTER surface temperature time series at the Merapi crater that was retrieved from Surface Kinetic Temperature (Product ID: AST_08v003); with a total of 287 cloud-free images out of 558 available scenes (USGS, 2016). The STL decomposition of the ASTER LST time series is displayed in Fig. 8. The one-decade trend (9.8 yrs. period) closely matched that (10.2 yrs. period) of the MODIS LST products (in Fig. 4), with a persistently upward trend. MODIS catches more thermal anomaly peaks caused by the eruptions than ASTER does because of its higher temporal resolution (the total number of valid images from MODIS is about two times that of ASTER). In a similar vein, ASTER catches other temperature peaks than MODIS due to its higher spatial resolution. The major advantage of MODIS is the subdaily acquisitions of images. Despite the lower spatial resolution, the higher temporal resolution does provide more detailed land surface information of the Merapi volcano. Statistical summary on the retrieved land surface temperature at Merapi crater both from ASTER and MODIS sensors is listed in Table 2. It indicates that MODIS acquired LSTs are generally 3 °C lower than those of ASTER. The discrepancy between ASTER and MODIS derived land surface temperatures can be attributed to the differences in spatial resolution and retrieval algorithms (Jacob et al., 2004; Liu et al., 2006). In general, the recorded secular-up trend of the MODIS LST time series is in agreement with the ASTER LST time series.

3.3. BT distribution of Merapi volcano obtained from Landsat imagery

The mean diameter of Merapi crater is around 500 m (see Fig. 1), however, the spatial resolution of the MODIS LST imagery is 1 km.

Thus MODIS, with a high temporal resolution but the low spatial resolution, is not ideal for detecting the detailed thermal features at the Merapi crater. However, the high-resolution Landsat TIR imagery (30 m pixels) is useful to delineate the spatial pattern of thermal anomalies on volcanic surfaces, although it suffers from a less than optimum temporal resolution. We have prescreened the Landsat archive (Landsat 5 TM and Landsat 7 ETM+) to process 118 scenes in order to obtain the BT images of Merapi, all of which had limited cloud contamination. Thirty-two scenes out of a total of 118 Landsat scenes are illustrated in Fig. A1 (see Online Resource) which shows the multitemporal BT distribution of Merapi crater from 1988 to 2019. Table A1 (see Online Resource) lists the corresponding statistics summary of brightness temperatures. A few exemplary scenes are also presented in Figs. 9 and 10. The pattern indicates that the surface temperature ranges in the study area with colour spanned from blue to red. Thermal anomaly areas are represented by distinct red colors. Thermally anomalous regions at the Merapi crater are generally 5–28 °C hotter than the surroundings. Thermal anomaly areas are in agreement with the locality of the debris ravines on the volcano's flanks which are indicated by the red colour.

Spatio-temporal temperature variations in Figs. 9 and 10 show that extents of thermal anomaly areas in the Merapi summit change over the time period of 1988–2019. Images in Figs. 9 and 10 are generally tainted by cloud coverage. However, the Merapi crater area is mostly clean as evidenced in the left-column optical imagery. Imagery sets from 1992 to 2018 reveal consistency in the temperature anomaly pattern of Merapi which is caused either by eruption events, or the surface/subsurface heat sources. Fig. 11 displays the 30 m spatial resolution zoomed-in Landsat images at Merapi summit area. The variations of the thermal area at the summit are the results of endogenous and exogenous eruptive processes, i.e., interactions of intrusive, effusive, and

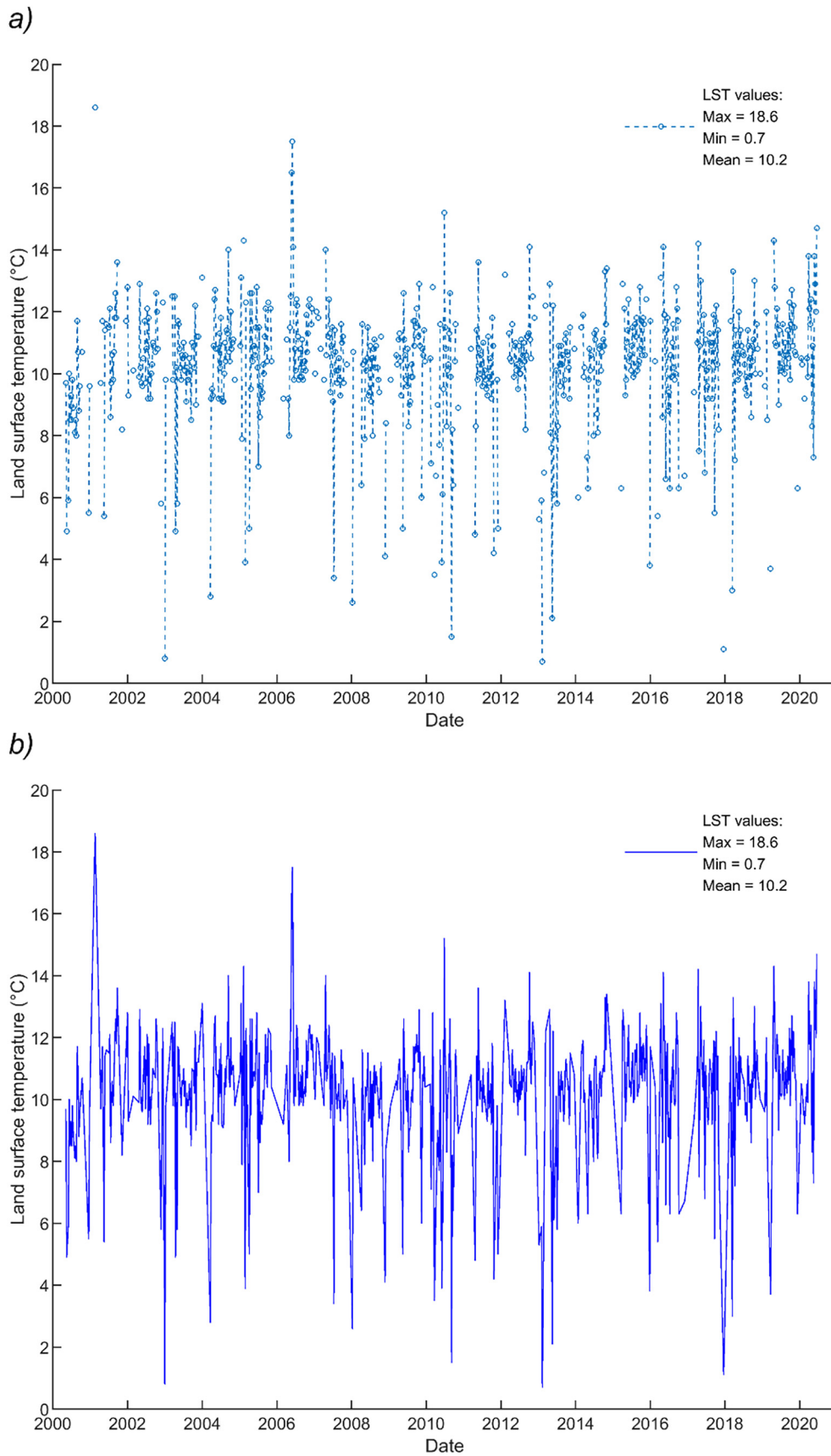


Fig. 4. LST temperature time series at Merapi crater (2910 m asl.). a) The nighttime 8-day average LST time series at Merapi crater from MODIS in the period March 2000 to June 2020. Note that gaps in the time series will be the result of cloud and/or the eruption plume masking the surface from 934 data points from the time period. b) MODIS LST time series with the data gaps excluded.

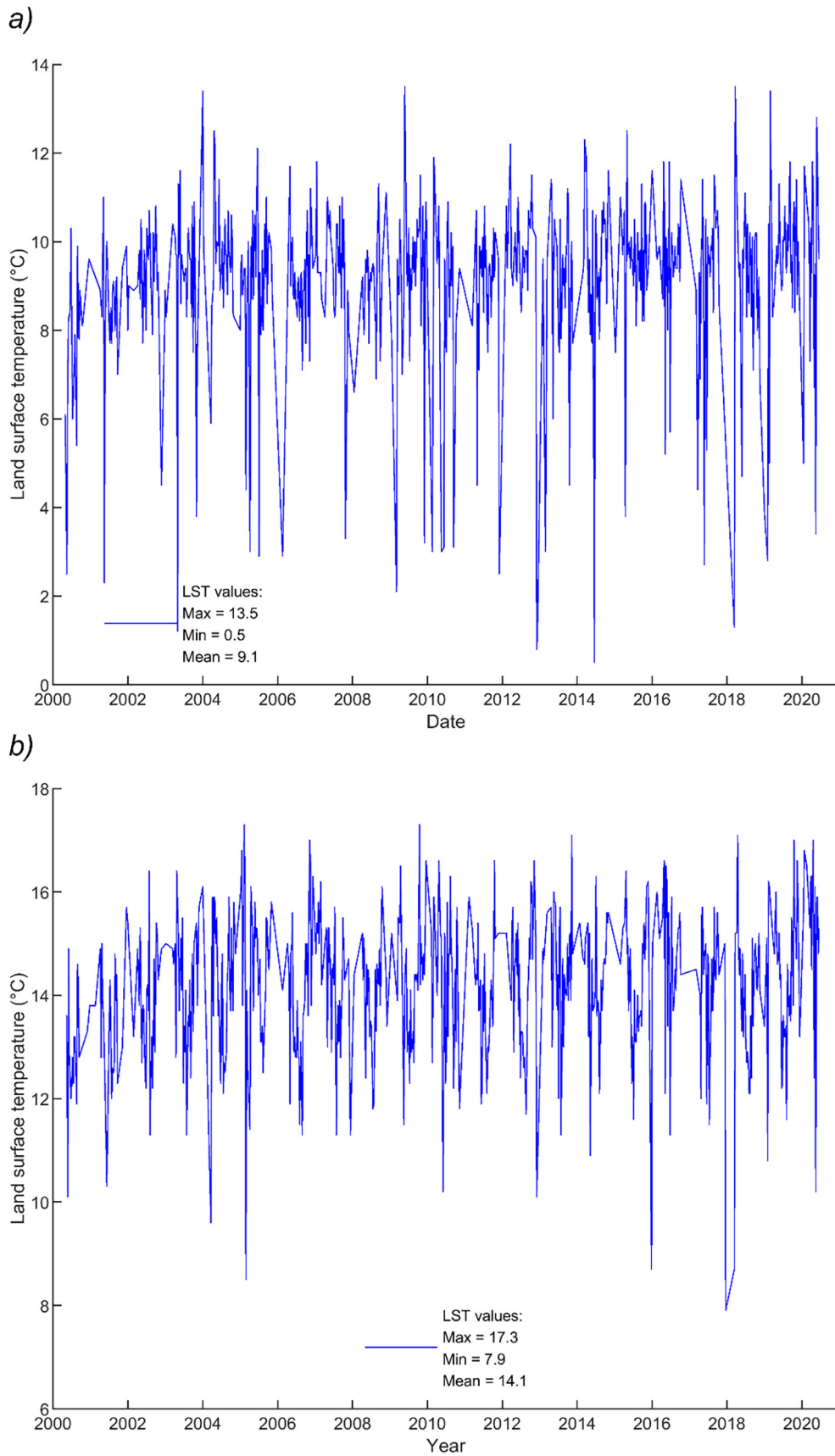


Fig. 5. Background temperature time series of adjacent areas nearby to the Merapi crater. The nighttime 8-day average LST time series at a) Merbabu crater (3118 m asl.) and b) saddle area in between the Merapi and Merbabu (around 1700 m asl.), from MODIS in the period March 2000 to June 2020.

Table 1

Results of independent t-test presenting significant differences between the mean LST of Merapi and that of Merbabu and Saddle areas. N: Number of the dataset; Df: degrees-of-freedom; P: *p*-value.

Axis	Category	N	Mean	t-test	Df	P
Merapi vs. Merbabu	Merapi LST	583	10.2	9.6 (right tail)*	1158	6.8e-21
	Merbabu LST	577	9.1			
Merapi vs. Saddle	Merapi LST	583	10.2	−36.8 (left tail)**	1166	4.7e-197
	Saddle LST	585	14.1			

* right tail – Test against the alternative hypothesis that the population mean of Merapi is greater than the population mean of Merbabu.

** left tail – Test against the alternative hypothesis that the population mean of Merapi is less than the population mean of Saddle.

explosive activity, either before, during, or after the volcanic eruptions (Delcamp et al., 2014). For instance, in the period of 1992–1995, 2000–2007, 2009–2012, and 2016–2018, the thermal anomaly area increased apparently because of the eruption events in 1994 (Abdurachman et al., 2000; Voight and Davis, 2000), 2006 (Carr et al., 2016; Ratdomopurbo et al., 2013), 2010 (Cronin et al., 2013; Komorowski et al., 2013; Mei et al., 2013), and 2018, respectively. The model of the conductivity structure along the volcano's north–south profile, as demonstrated by (Müller et al., 2002) shows, that magma distribution presumably would have to be quite shallow to have this effect. Thus these spatio-temporal surface temperature variations do provide important information regarding the activities of heat sources.

Due to the relative longer revisiting time (16-days) and frequent cloud contaminations, Landsat obtains fewer cloud-free images

compared to MODIS. However, the relative higher distinguishing ability indeed provides useful information on the pattern of thermal anomaly distribution on the volcano surface, which is essential for understanding the subsurface volcanic structures (i.e., Figs. 9–11). Such surface anomaly patterns are impossible to observe from the ground-based point measurements, considering either the site remoteness, accessibility, or the operational cost.

It is necessary to confirm that the positive thermal anomaly is not caused by the land use or land cover changes in Merapi area. Observation and analysis of the distribution of pyroclastic flow deposits for Merapi volcano throughout 2001–2017 show that the pyroclastic flow depositional area mainly resided in the southwestern region before the eruption in 2010 and migrated to the southern region after the 2010 eruption (Kadavi et al., 2017). However, no significant land use or land cover changes have happened in the area of Merapi crater ROI (see Figs. 1 and 11). The LST time series are extracted from imagery that covers a well-defined area around the crater of Merapi and not lower elevation areas that are subjected to human-related interventions.

4. Discussion

4.1. Seasonal component and trend component of STL decomposition on MODIS LST time series

Given that the seasonal period (1.02 years, Fig. 6) is close to the temperature annual cycle, a comparison with the near-surface on-site air temperature is carried out for detailed investigation of the seasonal component. The air temperature dataset is from the NASA Prediction of Worldwide Energy Resource (POWER) with the validated accuracy

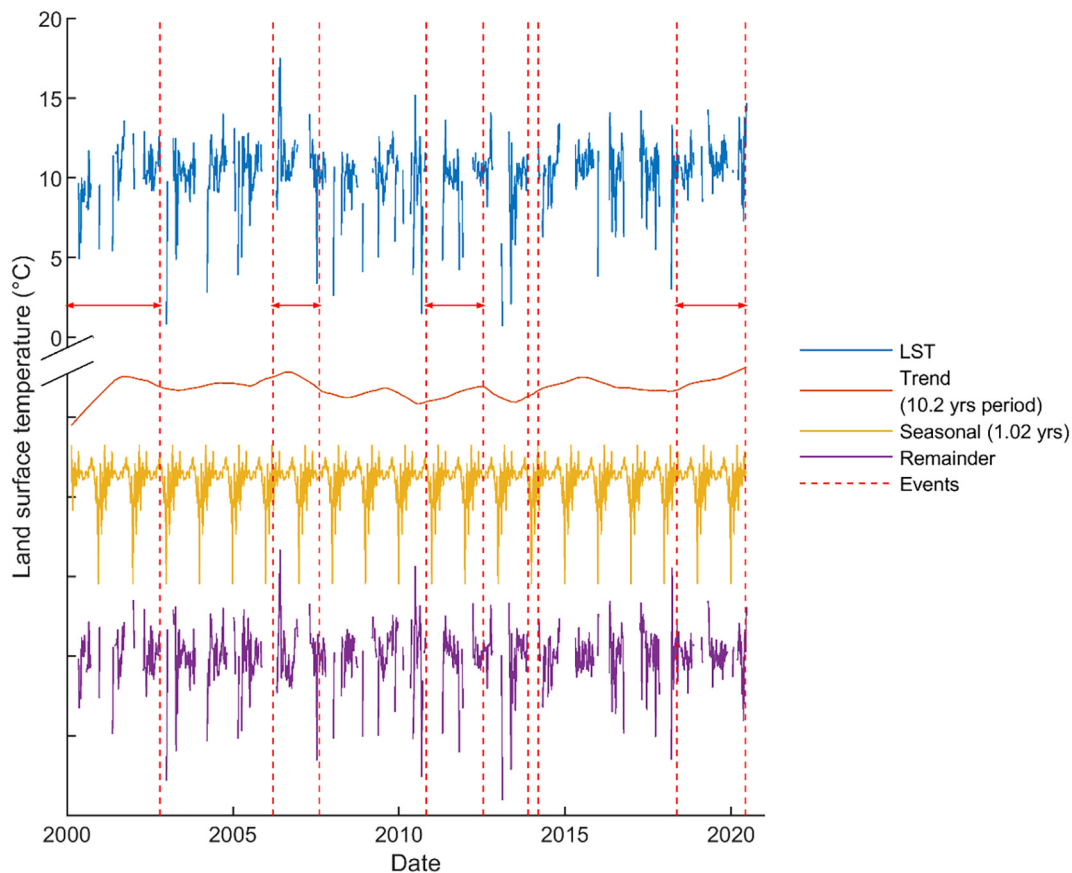


Fig. 6. STL Decomposition of MODIS LST series of Merapi crater. The Seasonal Trend Decomposition using Loess (STL) was used to divide up the MODIS LST time series into three parts namely: the trend, the seasonality, and the remainder. The vertical thin dashed red lines indicate the dates of recorded eruption events or volcanic unrest periods (i.e., events on Jun 21, 2020, 11 May 2018, 9 March 2014, 18 November 2013, 26 October 2010–15 July 2012, 16 March 2006–8 August 2007, and 20 January 1992–19 October 2002, respectively; horizontal double-headed arrows indicate the eruptive spans). The dominant periods for seasonal and trend are 1.02 years and 10.2 years from the Fourier transform calculation.

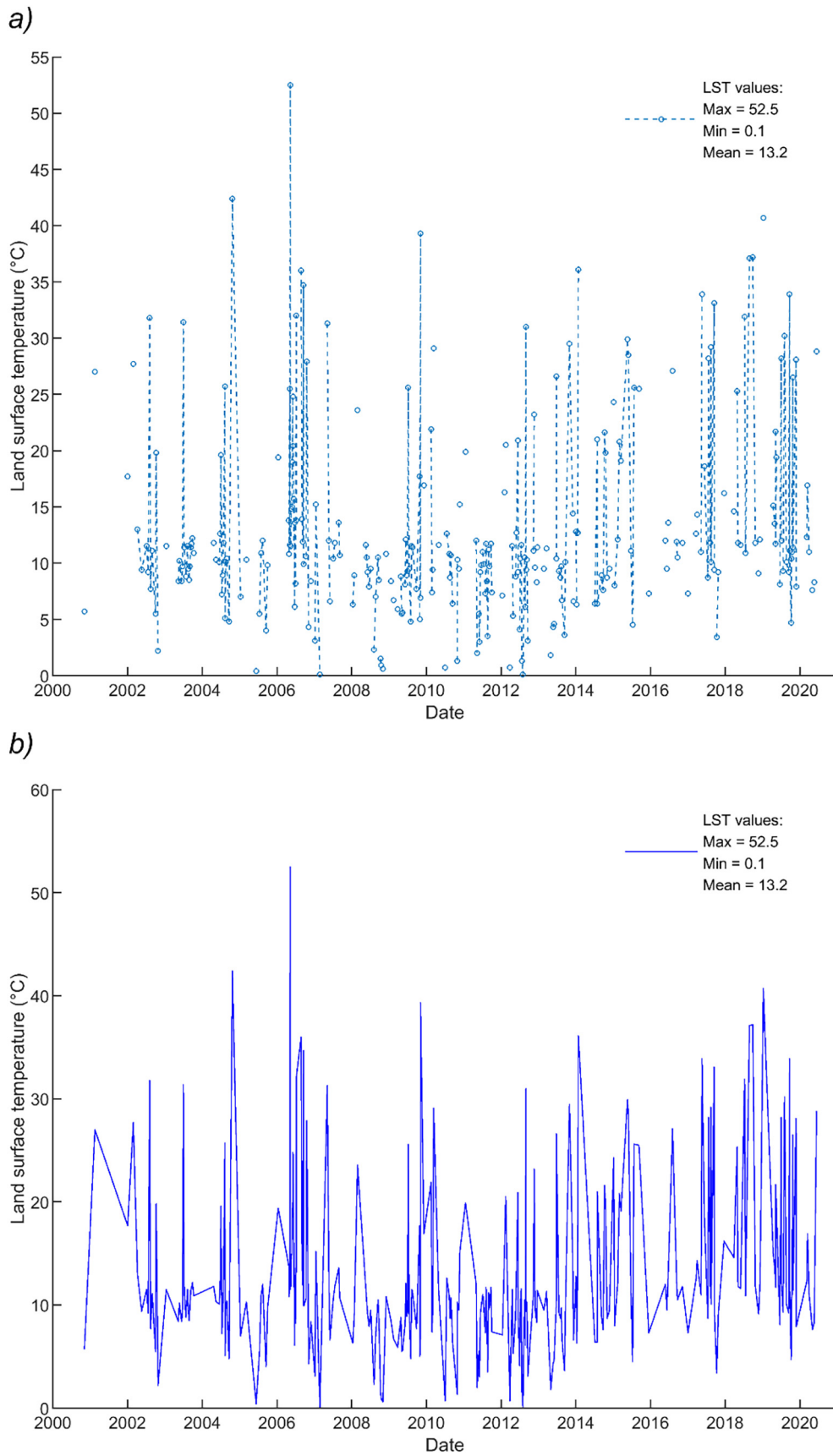


Fig. 7. Illustration of the ASTER daytime and nighttime LST at Merapi crater from March 2000 to June 2020. a) The ASTER LST time series. Note that gaps in the time series will be the result of cloud and/or the eruption plume masking the surface from 558 data points from the time period. b) ASTER LST time series with the data gaps excluded.

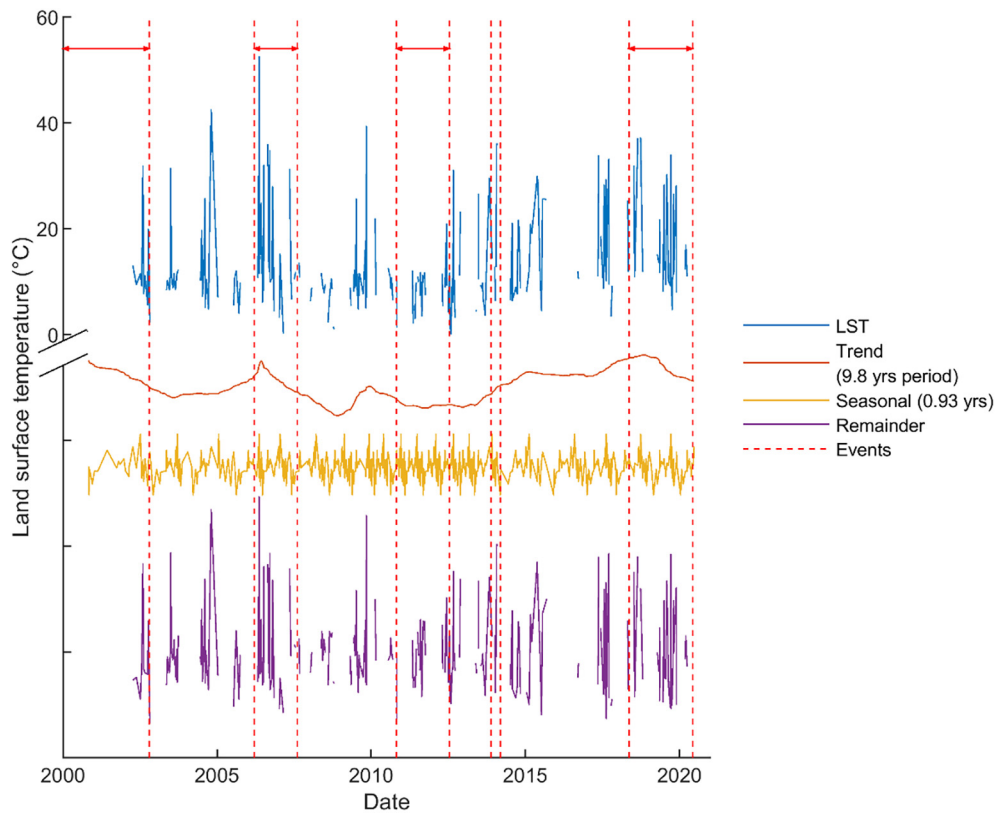


Fig. 8. STL Decomposition of ASTER LST series of Merapi crater. The Seasonal Trend Decomposition using Loess (STL) was used to divide up the ASTER LST time series into three parts namely: the trend, the seasonality, and the remainder. The vertical thin dashed red lines indicate the dates of recorded eruption events or volcanic unrest periods (i.e., events on Jun 21, 2020, 11 May 2018, 9 March 2014, 18 November 2013, 26 October 2010–15 July 2012, 16 March 2006–8 August 2007, and 20 January 1992–19 October 2002, respectively; horizontal double-headed arrows indicate the eruptive spans.). The dominant periods for seasonal and trend are 0.93 years and 9.8 years from the Fourier transform calculation. (For interpretation of the references to colour in this figure legend, the reader is referred to the web version of this article.)

range of ± 0.96 °C (Stackhouse Jr et al., 2018). The detrended on-site 8-day average air temperature has been utilized as a reference to the surface temperature annual cycle. Comparison between the LST seasonal component and the detrended annual-cycle air temperature is illustrated in Fig. A2a (see Online Resource) in its decomposed form. Kurtosis and skewness of each time series have been used for indicating the similarity level. The kurtosis and skewness measure the asymmetry or distortion and the height and sharpness relative to a normal distribution, respectively. The cross correlation is also calculated to compare the two time series in Fig. A2b (see Online Resource) which indicates a low level similarity. High similarity of these two signifies that the LST time series contained the climate annual cycles as its seasonal component. The low-similarity implies that the seasonal component has a low-level disturbance from other contributing factors such as volcano eruption and heat release. The large differences between the kurtosis and skewness values in Fig. A2 (see Online Resource) suggests the low-similarity between the LST seasonal component and the annual-cycle air temperature.

Table 2

Statistical summary of land surface temperature at Merapi crater from ASTER and MODIS sensors (2000–2020).

Satellite & Sensor	Total number of valid images	Min	LST (°C) Max	Mean	Acquisition time (local time)
Terra ASTER	287	0.1	52.5	13.2	night 10:30 pm/ day: 10:30 am
Terra/Aqua MODIS	586	0.7	18.6	10.2	Terra: 10:30 pm Aqua: 1:30 am

Fig. 12 demonstrates the trend of STL decomposition on the MODIS and ASTER LST time series (as derived from the data in Figs. 6 and 8). Both trends of the MODIS and ASTER LST time series appears to be gently increasing. The eruption events are not always corresponding to the high-temperature values and this is a consequence of missing temperature dataset due to cloud and/or the eruption plume masking the land surface. The detected long-term increase in both the MODIS and ASTER LST is based on the full duration of the dataset collected at Merapi. However, if the trends in Fig. 12 were evaluated from 2004 to 2011, they appear a decrease in LST. These periods of relatively high or low temperature in the time series may be caused by the different unrest level of Merapi. For instance, based on the Merapi bulletin reports from the global volcanism program, Smithsonian Institution, say, there were fewer pyroclastic flows and lava dome growth with intermittent ash plumes and rock avalanches in 2004–2011; however, there was an increasing unrest, i.e., several eruptions and elevated seismicity occurred in June 2011–December 2014 (GVP, 2013). Patterns of the MODIS and ASTER trend time series in Fig. 12 don't look to be correlated well. The difference in dataset numbers (i.e., dataset gaps), as well as the sensor's spatial resolution (1 km vs. 90 m; i.e., spatial scale mismatches), may be attributed to differences between these two time series.

4.2. Temporal temperature distribution of Merapi volcano from 1988 to 2019

MODIS LST time series shows a gentle uptrend of Merapi volcano from 2000 to 2020 based on the results of the STL decomposition. To further investigate and validate the trends and possible cyclic activity of Merapi, the 30-m Landsat BT time series in Merapi crater from 1988 to 2019 (includes 93 Landsat scenes in total) is plotted in Fig. 13. The

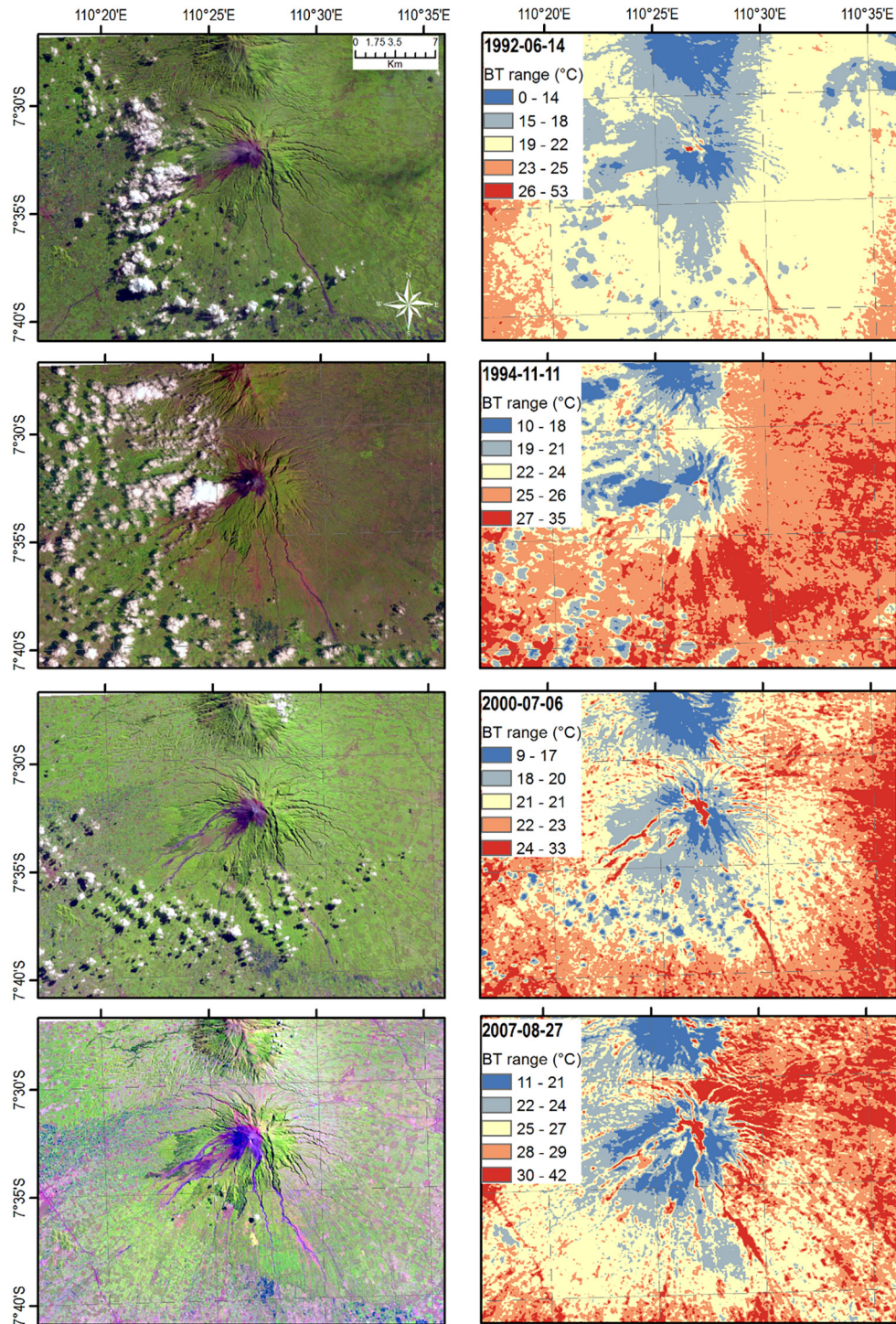


Fig. 9. The exemplary BT distribution pattern in Merapi crater from 1992 to 2018. The Landsat imagery (satellite and sensor ID: Landsat 5 TM, Landsat 7 ETM+) in the right column is the BT and the imagery in the left column are the corresponding optical (RGB) images. The top line in the legend box is the image acquisition date. Note that almost all the imagery has cloud contamination more or less.

BT values of the time series are extracted within the area of Merapi crater ROI (1 km by 1 km area as shown in Fig. 11) in each Landsat BT imagery. Landsat BT time series signifies an apparent uptrend with the linear trend slope of +0.22 °C per year. The recorded eruption events (date and VEI) are also plotted to visually assess the possible correlation between the temperatures variation and eruptions. The eruptions of 1990, 2002, 2006–2007 and 2010–2012 perfectly catch the high-temperature peaks locally, which indicate that the high temperature is

caused by the eruption events. However, the Volcanic Explosivity Index (VEI), which is a relative measurement for the explosiveness of volcanic eruptions, does not relate positively to the temperatures in all cases. For instance, the VEI of the 2010 eruption is 4, which is the largest during the last three decades (Borisova et al., 2013). However, the corresponding temperature to this event is not the highest. This phenomenon can be explained by the fact that major activities in Merapi are lava-dome extrusion, dome-collapse, and column-collapse pyroclastic

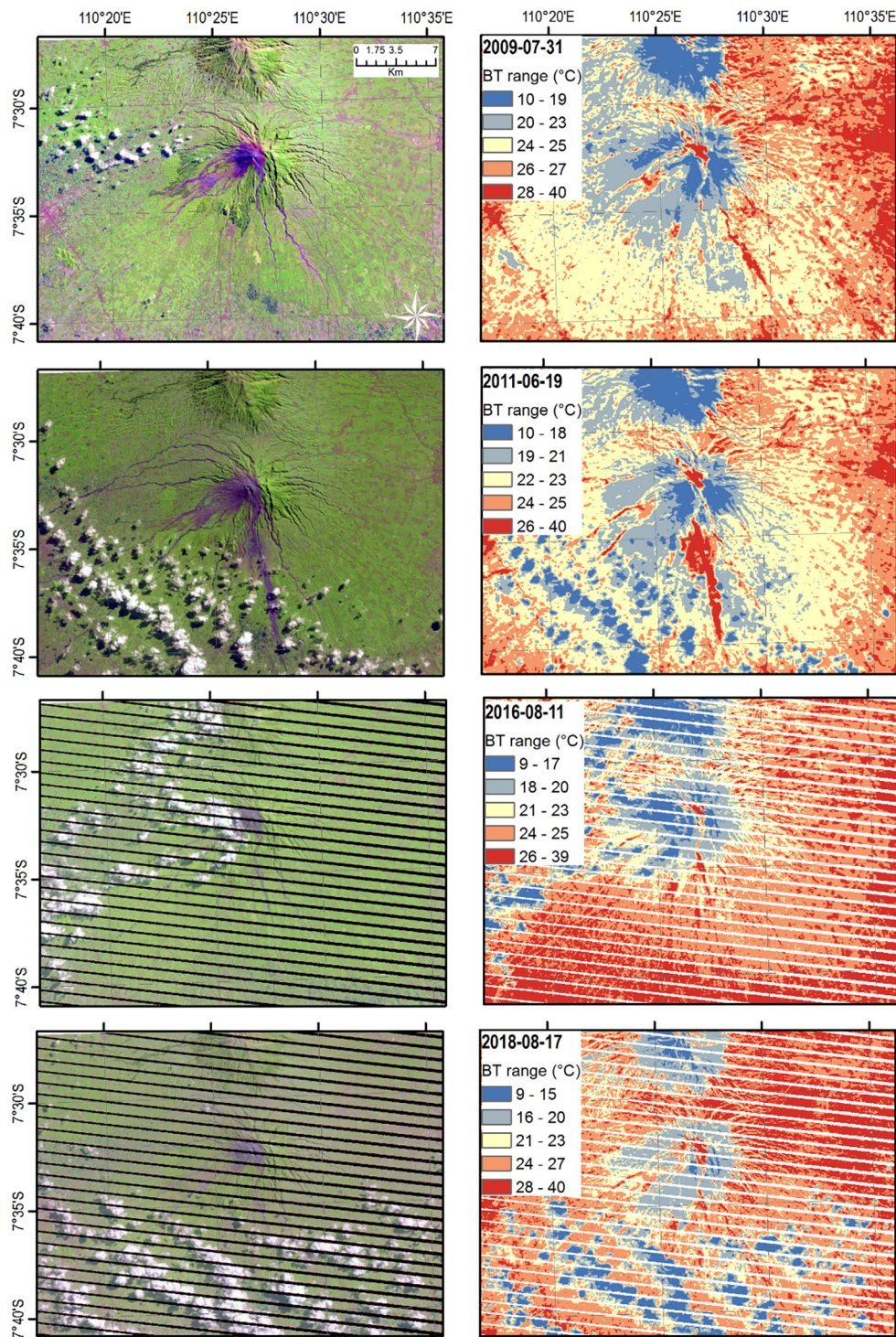


Fig. 10. (continued). Image stripes are from Landsat 7 ETM+ SLC-off images. Landsat 7 ETM+ SLC-off data is Landsat 7 images acquired after May 31, 2003, when the sensor's Scan Line Corrector (SLC) broke down. These image products have stripes and gaps, but are still useful and maintain the same radiometric and geometric qualities as data collected prior to the SLC malfunction (USGS, 2019).

flows (Wooster and Rothery, 1997). Theoretically, volcanic eruption styles depend on many factors, namely, the magma characteristics (including chemistry content, temperature, viscosity, volume, water and gas content), the presence of groundwater, and the plumbing system. Significantly however, the highest VEI eruptions do not necessarily lead to the highest surface temperatures and radiant emissions. This point is supported by previous study on satellite measurements of the thermal flux observed from 95 erupting volcanoes for the period of

2000 to 2014, in which it was shown that explosive volcanoes were consistently less emissive (Wright et al., 2015). Besides, there is an alternative explanation on how volcanic activity affects the thermal radiance of the land surface. Explosive eruptions generally are poorly captured in thermal images due to ash plumes obscuring the vent, whereas effusive eruptions actively emplace lava on the surface, which is easily detected, and over wider areas, by thermal sensors. Thus, the largest (explosive) eruption does not necessarily have the largest thermal signal. That is

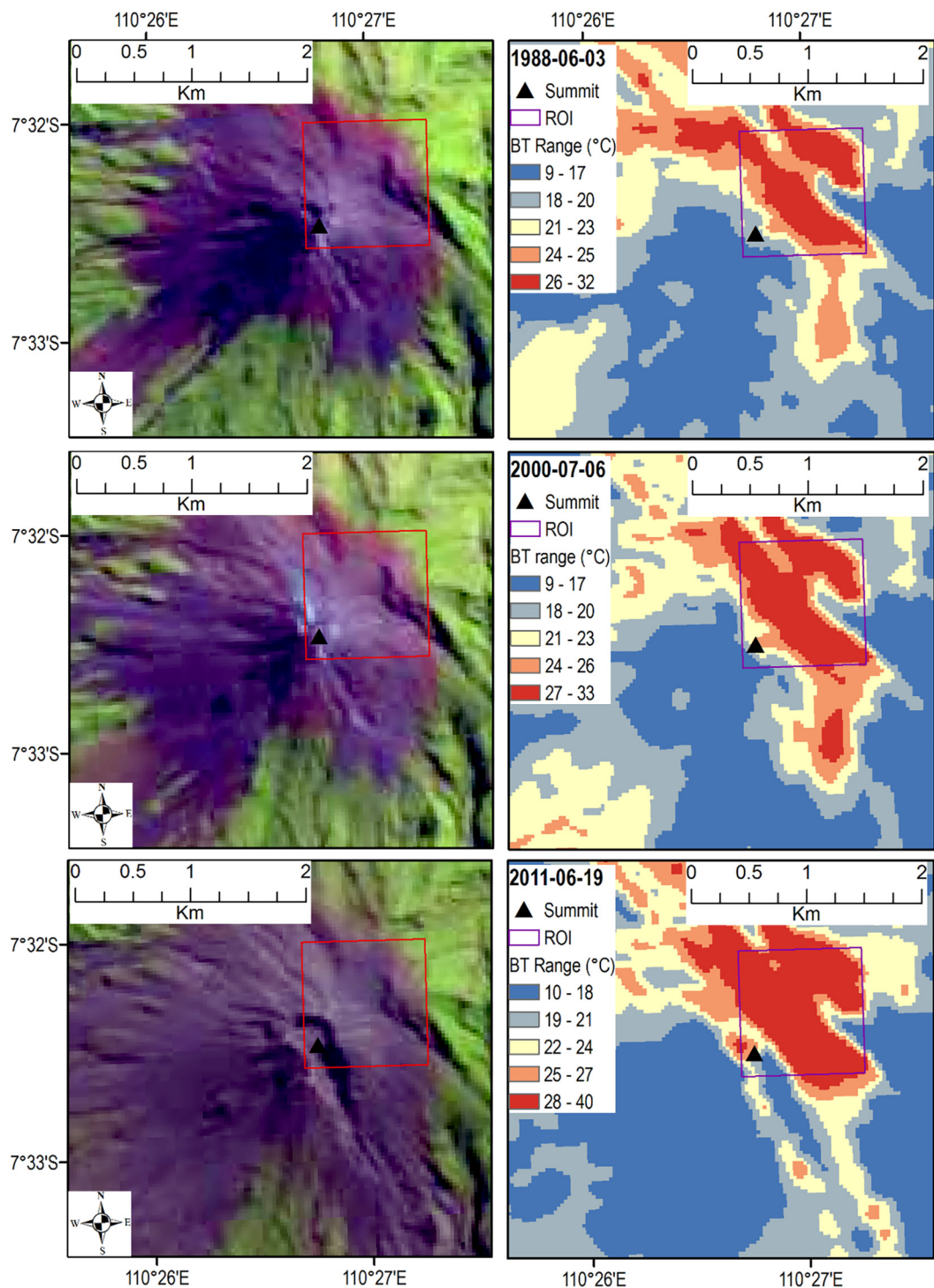


Fig. 11. The 30 m spatial resolution zooming Landsat images at Merapi summit area to display the thermal anomalous pattern. The right column are the thermal images and the left column are the corresponding optical (RGB) images. The top line in the legend box is the image acquisition date.

because effusive eruptions deposit lava in a manner easily detected by satellite thermal images, while explosive eruptions do not.

4.3. Spatial temperature distribution of Merapi volcano from 1988 to 2019

Change detection (pixel-by-pixel comparison) of Landsat BT distribution is performed to visualize the temperature spatial variation in Merapi. Fig. 14 shows the spatial variations in the temperature of the Merapi volcano from 1988 to 2019. The temperatures tend to increase

to the east and south of Merapi. Especially after the eruption events, such as the period of 1988–1990, 1992–1994, and 2007–2011, etc. These thermal anomalies are corresponding to the recorded eruption events on 10 October 1986–16 August 1990 (VEI = 2), 20 January 1992–19 October 2002 (VEI = 2), 16 March 2006–8 August 2007 (VEI = 1), and 26 October 2010–15 July 2012 (VEI = 4), respectively. In contrast, for the periods of 1996–2000, 2014–2015, and 2018–2019, in which no corresponding eruption events occur, the temperatures have no apparent increase to the east and south of Merapi. The

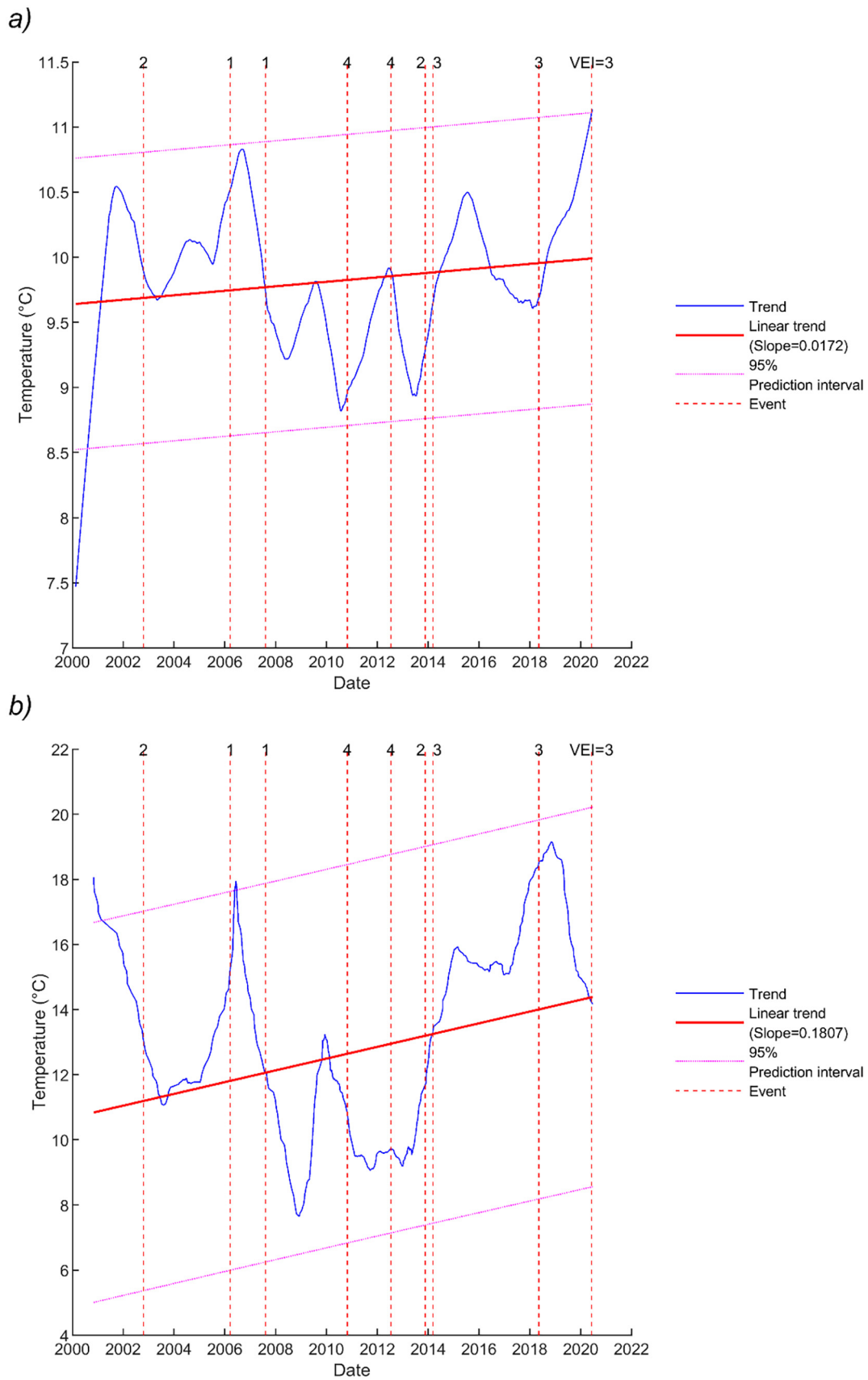


Fig. 12. a) The trend (slope = 0.0172 °C per year) component of STL decomposition on the MODIS LST time series (there is total 586 valid data points available). b) The trend (slope = 0.1807 °C per year) component of STL decomposition on the ASTER LST time series (there is total 287 valid data points available). The trend component is plotted as temperature and its linear fitted line is illustrated. The vertical thin dashed red lines indicate the dates of recorded eruption events. VEIs are marked aside. (For interpretation of the references to colour in this figure legend, the reader is referred to the web version of this article.)

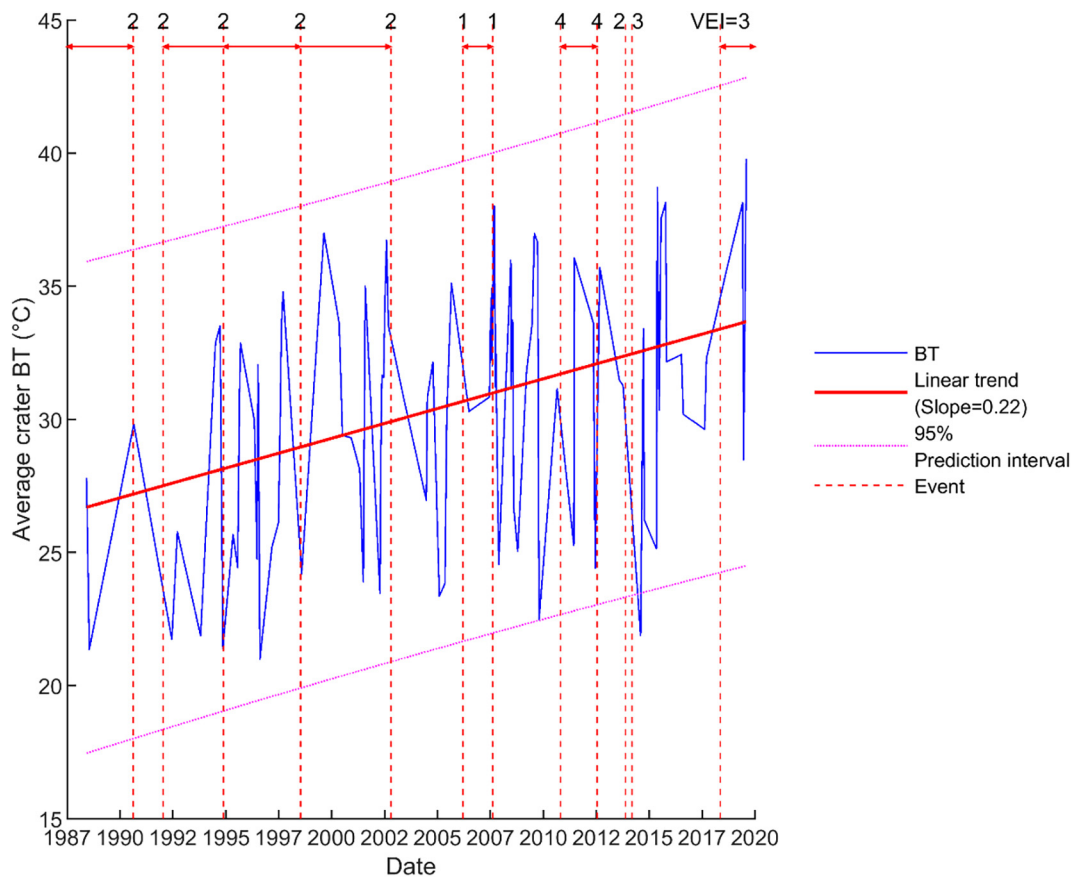


Fig. 13. Variations in average BT in Merapi crater ROI from 1988 to 2019. The vertical thin dashed red lines indicate the recorded eruption events on 11 May 2018 (VEI = 3), 9 March 2014 (VEI = 3), 18 November 2013 (VEI = 2), 26 October 2010–15 July 2012 (VEI = 4), 16 March 2006–8 August 2007 (VEI = 1), 22 November 1994–11 July 1998 (VEI = 2), 20 January 1992–19 October 2002 (VEI = 2), and 10 October 1986–16 August 1990 (VEI = 2), respectively. The horizontal double-headed arrows indicate the eruptive spans. VEIs are marked aside. The bold red line shows the increasing linear trend of crater temperature (slope = 0.2237 °C per year). The dotted lines show the 95% prediction interval. (For interpretation of the references to colour in this figure legend, the reader is referred to the web version of this article.)

eruption-related variation pattern signifies that the heat sources may be located at the east and south beneath Merapi.

To confirm that the spatial variations in temperature and positive thermal anomaly from the Landsat daytime temperature change detection at Merapi are of volcanic sources, we selected several cloud-free ASTER nighttime LST images for change detection analysis from the archive. The similar change detection (pixel-over-pixel comparison) operation is carried on the ASTER nighttime LST dataset as shown in Fig. 15. Results indicate that the nighttime surface temperature surrounding the volcano summit, which is less affected by the daytime insolation, generally increases in the period 2011–2018. Volcanic diffuse heating or surface warming (i.e., the diffuse heating of volcanic soils) is the dominant energy emitting of the Earth's internal heat during inter-eruptive periods of active volcanoes (Girona et al., 2021). Previous studies on the numerical model of heat conduction in active volcanoes show that it is possible to monitor magma activity underneath a volcano by detecting its surface temperature (Atmojo and Rosandi, 2015; Stevenson, 1992). The simulation is performed by solving numerically the temperature diffusion equation with complicated boundaries and a mixture of thermal properties of volcanic rocks.

It is noted that both Figs. 14 and 15 show that thermal anomalies at the area extent of 10 km within Merapi's summit can be affected by its plumbing system. The study on the influence of plumbing system structure on volcano dimensions and topography indicates that the height and basal radius of a volcano and its lavas can be used to estimate the fundamental properties of the plumbing system, specifically the depth and size of the magma chamber, i.e., the structure of the magmatic

system shapes the morphology of the volcanic edifice: 1) large volcanoes (>2000 m height and base radius > 10 km) usually are basaltic systems with over-pressured sources located at more than 15 km depth. 2) smaller volcanoes (<2000 m height and basal radius < 10 km) are associated with more evolved systems where the chambers feeding eruptions are located at shallower levels in the crust (<10 km) (Castruccio et al., 2017). Considering the height of Merapi is 2910 m asl, its base radius of magma plumbing system should be greater than 10 km, in which supports the phenomenon of 10-km-extent of thermal anomalous area surrounding summit in Figs. 14 and 15. Again, such observations on surface thermal anomaly patterns are impressive and interesting because they cannot be obtained from the in situ measurements.

The integration of subsurface model and surface measurements leads to a better understanding on the structure of active volcanoes. The prerequisite to such integration is data availability from both the conventional geophysical methods and remote sensing methods. It is an advantage of Merapi that its subsurface structure is well explored in previous geophysical studies. The magma plumbing system beneath Merapi was investigated by use of seismic tomography revealing strong S-velocity negative anomalies with amplitudes that reach -25% beneath Merapi and to the south. The resulting surface-wave tomography (S-wave model) and travel-time tomography in the East-West vertical profile show the negative anomalies to the east of Merapi (Koulakov et al., 2007; Koulakov et al., 2009; Koulakov et al., 2016; Luehr et al., 2013). Theoretically, areas of negative S-wave anomaly signify possible fluid sources (Koulakov, 2012). Besides seismic evidence, magnetic and

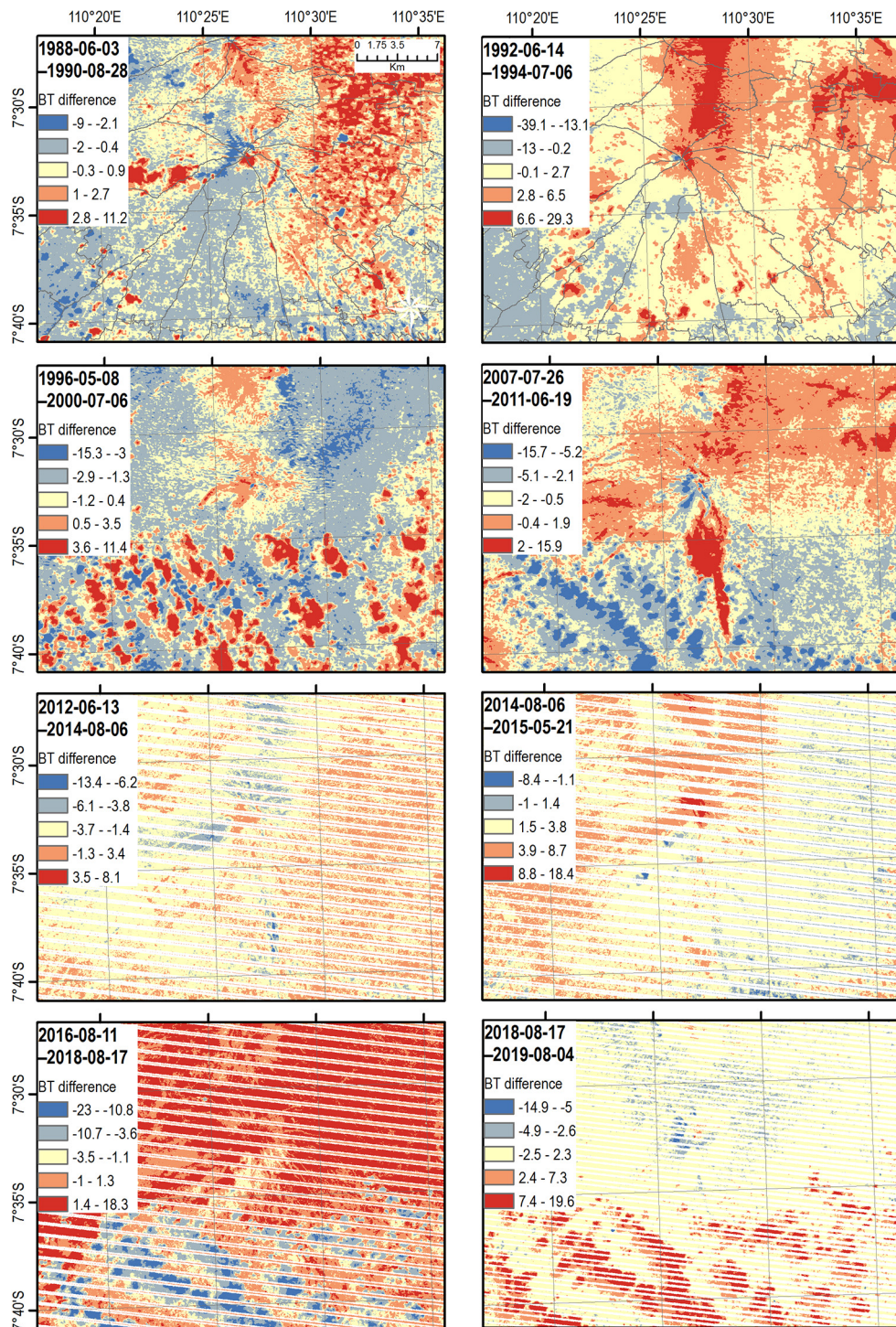


Fig. 14. Spatial variations in temperature–change detection (pixel-over-pixel comparison) of Landsat BT in Merapi volcano from 1988 to 2019.

resistivity measurements also provide useful information to delineate magma bodies. Hydrothermal bodies of low-resistivity below the summit and the south flank were identified by the electric resistivity tomography along with the north-south profile on Merapi (Byrdina et al., 2017; Commer et al., 2006). The magnitude of deep resistivity below the south flank is an order lower than that below the north. The stratified deposits detected in the south flank of Merapi separate the hydrothermal fluids—gas flows up to the crater and liquid flows down to the base (Byrdina et al., 2017; Müller et al., 2002). On-site temperature observations in the Woro and Gendol fumarolic fields of the

southeastern flank of Merapi indicate a persistent increase of very high (as high as 900 °C) temperatures which implies the proximity to the top of the heat sources which are seemingly evident in Fig. 14 (Allard and Tazieff, 1979; Jousset et al., 2012; Kavalieris, 1994; Richter et al., 2004; Tazieff, 1983).

Recently, Girona et al. (2021) have developed a new observable (i.e., median anomaly; δT) to track the heat release through volcano surfaces in order to verify the possible correlation between the surface heat emissions and pre-eruptive processes. They explored the temporal evolution of δT for five representative volcanoes around the world and

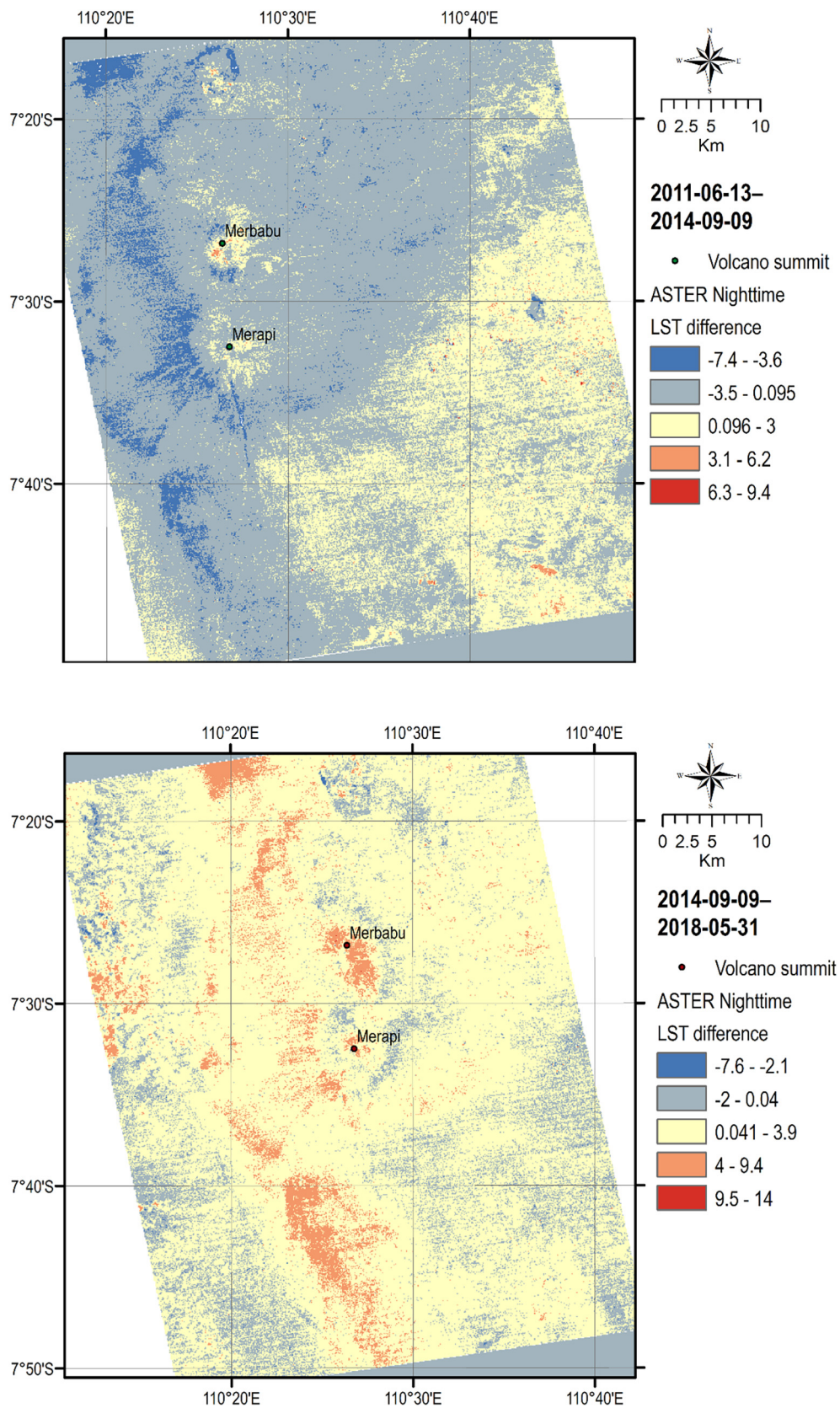


Fig. 15. Spatial variations in temperature—change detection (scene-specific pixel-by-pixel comparison) of ASTER Nighttime LST difference in Merapi volcano and the surrounding area. Note that the thermal anomalous patterns within 10 km of the volcanic summit can be the effects of the volcanic plumbing system.

proposed that the long-term pre-eruptive unrests reflect subsurface magmatic–hydrothermal fluid interactions (Girona et al., 2021). By the same token, we may attribute the temporal and spatial variations in surface temperatures of the Merapi volcano to the intensity variation of the underground hydrothermal activities. However, the detailed coupling process between the surface temperature and the subsurface groundwater temperature, the condensation of steam, and/or variations in soil properties and emissivity, etc. requires more effort in future investigation and studies.

The seismic, magnetic and resistivity measurements provide subsurface information to compare with the satellite remote sensed observations of Merapi. Fig. 16 illustrates the cross-section cartoon that depicts the surface fumaroles and subsurface features beneath Merapi according to the results of previous studies. It includes the stratified deposits detected in the south flank of Merapi, i.e., a large low-velocity anomaly beneath the southern flank of Merapi. This anomaly is divided into two layers. The upper layer is the 1-km thick volcanoclastic sedimentary cover. The lower layer of 4–8 km depths reflects a magma reservoir with partially molten rock. A low-velocity anomaly was observed as deep as 8 km beneath the Merapi summit that may be connected to the magma reservoir of Merapi (Koulakov et al., 2016). Fig. 16 also shows that the possible heat sources reside in the south and east of Merapi causing the positive thermal anomaly in the Woro and Gendol fumarolic fields of the southeastern flank of Merapi. The general mechanism is that the magma source is closer to the surface when eruptions occur, thus causing the positive thermal anomaly accordingly. The thermal anomaly observations from the satellite remote sensing serve as a verification for the results of the seismic and resistivity tomography, and vice versa.

In summary, satellite observed surface thermal anomaly features identified at Merapi may be the result of degassed shallow magma system (i.e., the flux of gas, heat, and/or hydrothermal systems), deep magma intrusions, and lava tongues or pyroclastic debris ravines. It is questionable to attribute all the surface anomaly features to the deep subsurface magma source, especially near the crater area, where lava tongues or debris ravines are distributed at a higher frequency. However, to separate the deep heat source of subsurface magma from that

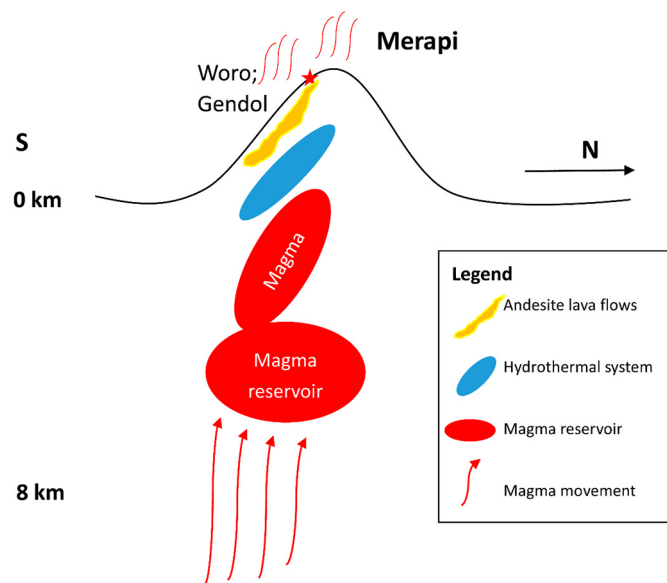


Fig. 16. The conceptual cross-section cartoon indicates that the possible magma sources reside in the south and east of Merapi volcano. Both the vertical scale and the topography along the profiles are exaggerated. The geophysical images indicate that the possible magma sources reside in the south and east of Merapi, which cause the positive thermal anomaly in the Woro and Gendol fumarolic fields (Allard and Tazieff, 1979; Camus et al., 2000) of the southeastern flank of Merapi (location marked with the red star). (For interpretation of the references to colour in this figure legend, the reader is referred to the web version of this article.)

of lava tongues and fresh pyroclastic flow deposits remains a challenge. Thus the surface thermal anomaly features observed by the satellite imagery are results of both the deep/shallow subsurface and surface heat contributions.

5. Conclusions

The observation and information on volcanoes from the bird's-eye view of a large area are generally not available via the conventional geophysical or geochemical measurements. Thus the satellite observed 2-D surface temperature information of a bigger scale area surrounding the volcanoes is appreciated. This study used a batch of satellite thermal images to detect and monitor the surface temperature at Merapi volcano. The crater temperature time series obtained is used to validate the past eruptions and assess the future eruptive trend of this volcano. Temporal and spatial temperature variations from 1988 to 2019 in Merapi are investigated through time series analysis and image change detection techniques. Temperature detections from both MODIS and Landsat thermal sensors indicate an overall increasing trend at Merapi crater. Specifically, LST trend based on STL decomposition of MODIS LST time series from 2000 to 2020 shows a gentle uptrend, and the trend based on the Landsat BT time series from 1988 to 2019 reveals a clear uptrend with the rate of $+0.22$ °C per year. Spatial variations in temperatures have been obtained from the pixel-over-pixel comparison on BT images of Merapi from 1988 to 2019. The resulting spatial change patterns are in line with those of the seismic and resistivity tomography, which indicate that the possible magma sources are located beneath the south and east flank of Merapi. Three satellite TIR imagery datasets, i.e., Landsat, MODIS, and ASTER, were analyzed in this study. The surface temperature tendency derived from all these satellite imageries indicates the longer term uptrend, which means that Merapi volcano will likely remain restless in future decades.

The satellite monitoring-based approach in this study is helpful to understand past events as well as the future eruption potential of Merapi. The retrieved temperature information is useful for volcano monitoring, hazard assessment and mitigation. Especially this method is most applicable in case the volcano is hard to access, or the budget of volcano monitoring is insufficient. Also, it is a compliment and suitable to be included with the existing volcanic monitoring systems for improving the monitoring tasks in Merapi volcano.

It is expected that remote sensing will play an increasingly important role in volcano monitoring and hazard mitigation as more near real-time observations become available nowadays. Recently, high temporal resolution geostationary infrared satellite data has been used for the real-time monitoring of eruptive styles, ash plume, and SO₂ clouds, etc. The versatile multispectral sensors are equipped onboard the geostationary satellite Meteosat Second Generation (MSG) or Himawari 8 (Bessho et al., 2016; Ishii et al., 2018; Lombardo et al., 2019; Marchese et al., 2018; Schmetz et al., 2005). These satellites can provide rapid scan imagery with a repeat cycle of 10 min, but observing only a third of the Earth's disk. Plus, the spatial resolution is rather coarse (2 km spatial resolution for thermal bands), which has hindered the application of volcano studies. Generally, sensors used for the infrared monitoring of volcanic activity is limited by the trade-offs between spatial and temporal resolutions. In addition, remote sensing is restricted to detecting the surficial and the shallow buried thermal sources. Thus, it cannot be considered as an all-powerful tool to explore and monitor volcanoes. The interdisciplinary approach including geology, geophysics, geochemistry, and remote sensing is the way to achieve better understanding on prediction, hazard management, and assessment of volcanoes in the future.

Funding

This research was financially supported by the Ministry of Science and Technology (MOST) of Taiwan, grant number MOST 108-2116-M-

008-011; 108-2811-M-008-576; 109-2116-M-008-010; 109-2811-M-008-549; 110-2116-M-008-016; 110-2811-M-008-559.

Author contributions

H.P.C. and K.K. conceived the research concept. H.P.C. performed the data processing and analysis, and wrote the manuscript. K.K. and M.B. supported development of work and contributed to the data interpretation and manuscript evaluation.

Declaration of Competing Interest

The authors declare no conflict of interest.

Acknowledgments

The Landsat images are provided from <https://lpdaac.usgs.gov/>. The MODIS 8-day average LST products are provided from the Global 1 km level-3 MODIS Land Surface Temperature and Emissivity (LST/E) 8-day datasets (MOD11A2 Collection 6), available from <https://ladsweb.modaps.eosdis.nasa.gov/>. The air temperature products are provided from the NASA Prediction of Worldwide Energy Resource (POWER), available from <https://power.larc.nasa.gov/data-access-viewer/>. Last but not least, we truly appreciate the Editor Diana C. Roman and two anonymous reviewers for their constructive comments.

Appendix A. Supplementary data

Supplementary data to this article can be found online at <https://doi.org/10.1016/j.jvolgeores.2021.107405>.

References

- Abdurachman, E., Bourdier, J.-L., Voight, B., 2000. Nuées ardentes of 22 November 1994 at Merapi volcano, Java, Indonesia. *J. Volcanol. Geotherm. Res.* 100, 345–361.
- Ahmad, S., Salomonson, V., Barnes, W., Xiong, X., Leptoukh, G., Serafino, G., 2002. P1. 6 Modis Radiances and Reflectances for Earth System Science Studies and Environmental Applications.
- Allard, P., Tazieff, H., 1979. Phenomenologie et Cartographie Thermique Des Principales Zones Fumerolliennes du Volcan Merapi (Indonesie): Phenomenology and Thermal Mapping of the Principal Fumarole Zones of Merapi Volcano. Indonesia.
- Artis, D.A., Carnahan, W.H., 1982. Survey of emissivity variability in thermography of urban areas. *Remote Sens. Environ.* 12, 313–329.
- Atmojo, A.A., Rosandi, Y., 2015. Numerical model of heat conduction in active volcanoes induced by magmatic activity. AIP Conference Proceedings. vol 1. AIP Publishing LLC, p. 080005.
- Barsi, J.A., Barker, J.L., Schott, J.R., 2003. An atmospheric correction parameter calculator for a single thermal band earth-sensing instrument. IGARSS 2003. 2003 IEEE International Geoscience and Remote Sensing Symposium. Proceedings (IEEE Cat. No. 03CH37477). IEEE, pp. 3014–3016.
- Bessho, K., et al., 2016. An introduction to Himawari-8/9—Japan's new-generation geostationary meteorological satellites. *J. Meteorol. Soc. Japan Ser II* 94, 151–183.
- Bignami, C., Ruch, J., Chini, M., Neri, M., Buongiorno, M.F., Hidayati, S., Sayudi, D.S., 2013. Pyroclastic density current volume estimation after the 2010 Merapi volcano eruption using X-band SAR. *J. Volcanol. Geotherm. Res.* 261, 236–243.
- Borisova, A.Y., et al., 2013. Highly explosive 2010 Merapi eruption: evidence for shallow-level crustal assimilation and hybrid fluid. *J. Volcanol. Geotherm. Res.* 261, 193–208.
- Byrdina, S., Friedel, S., Vandemeulebrouck, J., Budi-Santoso, A., Suryanto, W., Rizal, M., Winata, E., 2017. Geophysical image of the hydrothermal system of Merapi volcano. *J. Volcanol. Geotherm. Res.* 329, 30–40.
- Camus, G., Gourgaud, A., Mossand-Berthommier, P.-C., Vincent, P.-M., 2000. Merapi (Central Java, Indonesia): an outline of the structural and magmatological evolution, with a special emphasis to the major pyroclastic events. *J. Volcanol. Geotherm. Res.* 100, 139–163.
- Carr, B.B., Clarke, A.B., Vanderkluyzen, L., 2016. The 2006 lava dome eruption of Merapi Volcano (Indonesia): detailed analysis using MODIS TIR. *J. Volcanol. Geotherm. Res.* 311, 60–71.
- Castruccio, A., Diez, M., Gho, R., 2017. The influence of plumbing system structure on volcano dimensions and topography. *J. Geophys. Res. Solid Earth* 122, 8839–8859.
- Chadwick, J.P., Troll, V.R., Ginibre, C., Morgan, D., Gertisser, R., Waight, T.E., Davidson, J.P., 2007. Carbonate assimilation at Merapi Volcano, Java, Indonesia: insights from crystal isotope stratigraphy. *J. Petrol.* 48, 1793–1812.
- Chan, H.-P., Chang, C.-P., 2018. Exploring and monitoring geothermal and volcanic activity using Satellite Thermal Infrared data in TVG, Taiwan. *Terr. Atmos. Ocean. Sci.* 29, 1–18. <https://doi.org/10.3319/TAO2018012201>.
- Chan, H.-P., Chang, C.-P., Dao, P.D., 2017. Geothermal anomaly mapping using landsat ETM+ data in Ilan Plain, Northeastern Taiwan. *Pure Appl. Geophys.* 1–21.
- Cleveland, R.B., Cleveland, W.S., McKee, J.E., Terpenning, I., 1990. STL: a seasonal-trend decomposition. *J. Off. Stat.* 6, 3–73.
- Commer, M., Helwig, S.L., Hördt, A., Scholl, C., Tezkan, B., 2006. New results on the resistivity structure of Merapi Volcano (Indonesia), derived from three-dimensional restricted inversion of long-offset transient electromagnetic data. *Geophys. J. Int.* 167, 1172–1187.
- Cronin, S.J., Lube, G., Dayudi, D.S., Sumarti, S., Subrandiyo, S., 2013. Insights into the October–November 2010 Gunung Merapi eruption (Central Java, Indonesia) from the stratigraphy, volume and characteristics of its pyroclastic deposits. *J. Volcanol. Geotherm. Res.* 261, 244–259.
- CVGHM, 2019. Centre for Volcanology and Geological Hazard Mitigation (CVGHM) (Pusat Vulkanologi & Mitigasi Bencana Geologi) (Formerly Volcanological Survey of Indonesia). Retrieved from <http://www.vsi.esdm.go.id/>.
- Darmawan, H., Walter, T.R., Troll, V.R., Budi-Santoso, A., 2018. Structural weakening of the Merapi dome identified by drone photogrammetry after the 2010 eruption. *Nat. Hazards Earth Syst. Sci.* 18, 3267–3281.
- Delcamp, A., de Vries, B.V.W., Stéphane, P., Kervyn, M., 2014. Endogenous and exogenous growth of the monogenetic Lemptégy volcano, Chaîne des Puys, France. *Geosphere* 10, 998–1019.
- Gertisser, R., Charbonnier, S.J., Keller, J., Quidelleur, X., 2012. The geological evolution of Merapi volcano, Central Java, Indonesia. *Bull. Volcanol.* 74, 1213–1233.
- Girona, T., Realmuto, V., Lundgren, P., 2021. Large-scale thermal unrest of volcanoes for years prior to eruption. *Nat. Geosci.* 14, 238–241.
- Gupta, R.P., 2017. *Remote Sensing Geology*. Springer.
- GVP, 2013. In: Venkze, E. (Ed.), Global Volcanism Program, 2013. Merapi (263250) in Volcanoes of the World, v. 4.8.5. Smithsonian Institution Downloaded 24 October 2020.
- Hafen, R.P., 2010. Local Regression Models: Advancements, Applications, and New Methods. Purdue University.
- Hamilton, W.B., 1979. Tectonics of the Indonesian Region. vol. 1078. US Govt. Print. Off.
- Harris, A., 2013. Thermal Remote Sensing of Active Volcanoes: A user's Manual. Cambridge university press.
- Harris, A.J., Rippepe, M., 2007. Regional earthquake as a trigger for enhanced volcanic activity: evidence from MODIS thermal data. *Geophys. Res. Lett.* 34.
- Huang, N.E., Wu, Z., 2008. A review on Hilbert–Huang transform: method and its applications to geophysical studies. *Rev. Geophys.* 46.
- Ishii, K., Hayashi, Y., Shimbori, T., 2018. Using Himawari-8, estimation of SO₂ cloud altitude at Aso volcano eruption, on October 8, 2016. *Earth Planets Space* 70, 19.
- Jacob, F., Petitcolin, F.O., Schmugge, T., Vermote, E., French, A., Ogawa, K., 2004. Comparison of land surface emissivity and radiometric temperature derived from MODIS and ASTER sensors. *Remote Sens. Environ.* 90, 137–152.
- Jousset, P., et al., 2012. The 2010 explosive eruption of Java's Merapi volcano—a '100-year' event. *J. Volcanol. Geotherm. Res.* 241, 121–135.
- Kadavi, P., Lee, W.-J., Lee, C.-W., 2017. Analysis of the pyroclastic flow deposits of mount Sinabung and Merapi using Landsat imagery and the artificial neural networks approach. *Appl. Sci.* 7, 935.
- Kavaleris, I., 1994. High Au, Ag, Mo, Pb, V and W content of fumarolic deposits at Merapi volcano, central Java, Indonesia. *J. Geochem. Explor.* 50, 479–491.
- Komorowski, J.-C., et al., 2013. Paroxysmal dome explosion during the Merapi 2010 eruption: processes and facies relationships of associated high-energy pyroclastic density currents. *J. Volcanol. Geotherm. Res.* 261, 260–294.
- Koulakov, I., 2012. Multiscale seismic tomography imaging of volcanic complexes. Updates in Volcanology—A Comprehensive Approach to Volcanological Problems. IntechOpen.
- Koulakov, I., et al., 2007. P and S velocity structure of the crust and the upper mantle beneath central Java from local tomography inversion. *J. Geophys. Res. Solid Earth* 112.
- Koulakov, I., Jakovlev, A., Luehr, B.G., 2009. Anisotropic structure beneath Central Java from local earthquake tomography. *Geochem. Geophys. Geosyst.* 10.
- Koulakov, I., et al., 2016. Structure of magma reservoirs beneath Merapi and surrounding volcanic centers of Central Java modeled from ambient noise tomography. *Geochem. Geophys. Geosyst.* 17, 4195–4211.
- Kubaneck, J., Westerhaus, M., Schenk, A., Aisyah, N., Brotopuspito, K.S., Heck, B., 2015. Volumetric change quantification of the 2010 Merapi eruption using TanDEM-X InSAR. *Remote Sens. Environ.* 164, 16–25.
- Li, Z.-L., et al., 2013. Satellite-derived land surface temperature: current status and perspectives. *Remote Sens. Environ.* 131, 14–37.
- Liu, Y., Hiyama, T., Yamaguchi, Y., 2006. Scaling of land surface temperature using satellite data: a case examination on ASTER and MODIS products over a heterogeneous terrain area. *Remote Sens. Environ.* 105, 115–128.
- Lombardo, V., Corradini, S., Musacchio, M., Silvestri, M., Taddeucci, J., 2019. Eruptive styles recognition using high temporal resolution geostationary infrared satellite data. *Remote Sens.* 11, 669.
- Luehr, B.-G., et al., 2013. Fluid ascent and magma storage beneath Gunung Merapi revealed by multi-scale seismic imaging. *J. Volcanol. Geotherm. Res.* 261, 7–19.
- Marchese, F., Falconieri, A., Pergola, N., Tramutoli, V., 2018. Monitoring the Agung (Indonesia) Ash Plume of November 2017 by means of infrared Himawari 8 data. *Remote Sens.* 10, 919.
- Mei, E.T.W., et al., 2013. Lessons learned from the 2010 evacuations at Merapi volcano. *J. Volcanol. Geotherm. Res.* 261, 348–365.
- Müller, M., Hördt, A., Neubauer, F., 2002. Internal structure of Mount Merapi, Indonesia, derived from long-offset transient electromagnetic data. *J. Geophys. Res. Solid Earth* 107, ECV 2–1–ECV 2–14.
- NASA, 2018. Status for: Land Surface Temperature and Emissivity (MOD11). General Accuracy Statement Retrieved from <https://modis-landsgfscnasagov/ValStatus.php?ProductID=MOD11>.

- NASA, 2019. Thermal Infrared Sensor (TIRS). Retrieved from <https://landsatgsfc.nasa.gov/thermal-infrared-sensor-tirs/>.
- NASA, 2020. Terra instruments. ASTER (Advanced Spaceborne Thermal Emission and Reflection Radiometer) Retrieved 16 May 2020 from <https://terra.nasa.gov/about/terra-instruments/aster>.
- Newhall, C., et al., 2000. 10,000 years of explosive eruptions of Merapi Volcano, Central Java: archaeological and modern implications. *J. Volcanol. Geotherm. Res.* 100, 9–50.
- Peng, X., Wu, W., Zheng, Y., Sun, J., Hu, T., Wang, P., 2020. Correlation analysis of land surface temperature and topographic elements in Hangzhou, China. *Sci. Rep.* 10, 1–16.
- Ratdomopurbo, A., Beauducel, F., Subandriyo, J., Nandaka, I.M.A., Newhall, C.G., Sayudi, D.S., Suparwaka, H., 2013. Overview of the 2006 eruption of Mt. Merapi. *J. Volcanol. Geotherm. Res.* 261, 87–97.
- Richter, G., Wassermann, J., Zimmer, M., Ohrnberger, M., 2004. Correlation of seismic activity and fumarole temperature at the Mt. Merapi volcano (Indonesia) in 2000. *J. Volcanol. Geotherm. Res.* 135, 331–342.
- Saepuloh, A., Urai, M., Aisyah, N., Widiwijayanti, C., Jousset, P., 2013. Interpretation of ground surface changes prior to the 2010 large eruption of Merapi volcano using ALOS/PALSAR, ASTER TIR and gas emission data. *J. Volcanol. Geotherm. Res.* 261, 130–143.
- Schmetz, J., Govaerts, Y., König, M., Lutz, H.-J., Ratier, A., Tjemkes, S., 2005. A Short Introduction to METEOSAT Second Generation (MSG) CIRA. Colorado State Univ, Fort Collins.
- Sobrino, J.A., et al., 2008. Land surface emissivity retrieval from different VNIR and TIR sensors. *IEEE Trans. Geosci. Remote Sens.* 46, 316–327.
- Stackhouse Jr., P.W., et al., 2018. POWER Release 8.0.1 (with GIS Applications) Methodology (Data Parameters, Sources, & Validation) Documentation Date December 12, 2018 (All previous versions are obsolete)(Data Version 8.0.1; Web Site Version 1.1.0).
- Stevenson, D.S., 1992. Heat Transfer in Active Volcanoes: Models of Crater Lake Systems. The Open University.
- Sun, C., Kong, F., Yin, H., Ren, Y., 2014. Analysis of factors affecting mountainous land surface temperature in the summer: a case study over Mount Tai. *Acta Ecol. Sin.* 34, 3396–3404.
- Tang, H., Li, Z.-L., 2013. Quantitative Remote Sensing in Thermal Infrared: Theory and Applications. Springer Science & Business Media.
- Tazieff, H., 1983. Monitoring and interpretation of activity on Mt. Merapi, Indonesia, 1977–1980: an example of practical, «Civil Defense», volcanology. *Forecasting Volcanic Events*, pp. 485–494.
- USGS, 2016. AST_08 v003. ASTER L2 Surface Kinetic Temperature Retrieved 20 March 2020 from https://lpdaac.usgs.gov/products/ast_08v003/.
- USGS, 2019. What is Landsat 7 ETM+ SLC-off data?. Retrieved from https://www.usgs.gov/faqs/what-landsat-7-etm-slc-off-data?qt-news_science_products=0#qt-news_science_products
- USGS, 2021. The USGS Global Visualization Viewer (GloVis). Retrieved from <https://glovis.usgs.gov/>.
- Vidal, A., Devaux-Ros, C., Moran, M.S., 1997. Atmospheric correction of Landsat TM thermal band using surface energy balance. *Remote Sens. Rev.* 15, 23–33.
- Voight, B., Davis, M., 2000. Emplacement temperatures of the November 22, 1994 nuée ardente deposits, Merapi Volcano, Java. *J. Volcanol. Geotherm. Res.* 100, 371–377.
- Walter, T., et al., 2015. Volcano-tectonic control of Merapi's lava dome splitting: the November 2013 fracture observed from high resolution TerraSAR-X data. *Tectonophysics* 639, 23–33.
- Wan, Z., 2014. New refinements and validation of the collection-6 MODIS land-surface temperature/emissivity product. *Remote Sens. Environ.* 140, 36–45.
- Wan, Z., Li, Z.-L., 1997. A physics-based algorithm for retrieving land-surface emissivity and temperature from EOS/MODIS data. *IEEE Trans. Geosci. Remote Sens.* 35, 980–996.
- Wooster, M., Rothery, D., 1997. Thermal monitoring of Lascar Volcano, Chile, using infrared data from the along-track scanning radiometer: a 1992–1995 time series. *Bull. Volcanol.* 58, 566–579.
- Wright, R., Blakett, M., Hill-Butler, C., 2015. Some observations regarding the thermal flux from Earth's erupting volcanoes for the period of 2000 to 2014. *Geophys. Res. Lett.* 42, 282–289.